CHAPTER 5

RESULTS

5 Results

5.1 DNA barcoding

The DNA extracted from the leaf of *N. herpeticum* was subjected to PCR amplification with rbcL as the target. Suitable primers (both forward and reverse) were used for analysis in a PCR unit. The forward and reverse primer sequence were ATGTCACCACAAACAGAGACTAAAGC and TCGCATGTACCTGCAGTAGC, respectively, from 5′→3′ end. The sequencing results were subjected to BLAST analysis, and the collected sample was confirmed as *N. herpeticum*. Subsequently, the nucleotide sequence was submitted to the GenBank repository, which can be accessed using accession number OP121185 (**Fig. 8**).

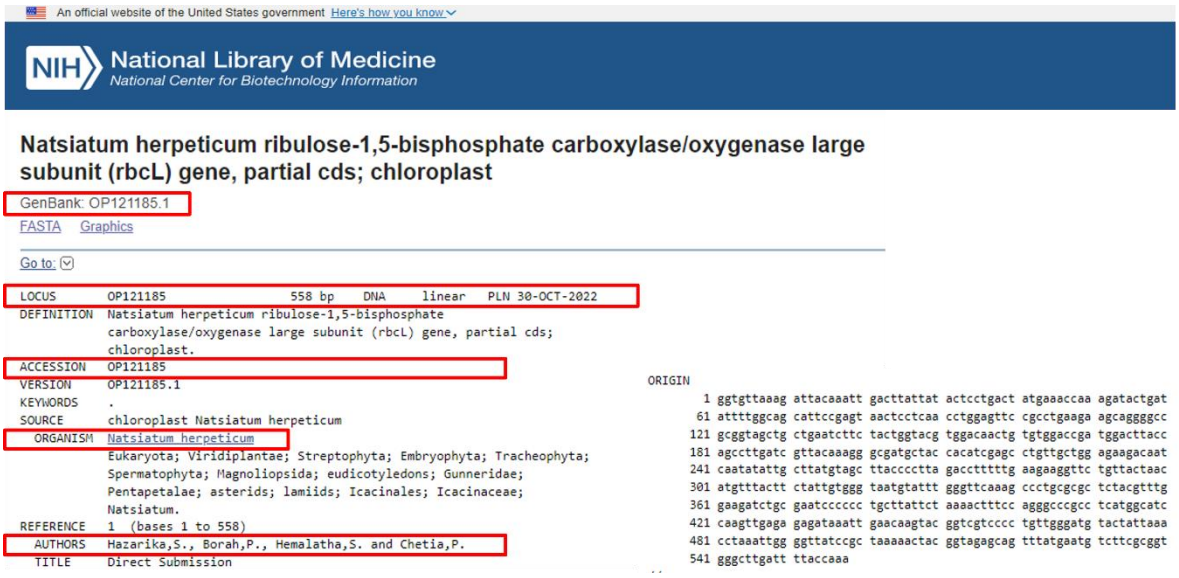

Fig. 8 A representation of GenBank database accessed with accession no. OP121185

5.2 Quality control assessment

The macroscopic analysis showed the leaf to be broadly ovate, cordate to truncate-shaped (dimension: 15-20 x 10-15 cm) containing rough lamina and white hairs on the surface (**Table 1**. The microscopical features of the leaf midrib, leaf petiole, and root of *N. herpeticum* are represented in **Fig. 9(A-F)**.

A transverse section through the leaf lamina revealed a dorsiventral structure with palisade mesophyll on the top layer and spongy parenchyma on the bottom layer, both covered by a thin layer of epidermis (**Fig. 9A**). In the lamina section, lignified xylem vessels with scalariform thickening were detected (**Fig. 9B**). The single-layer lower and upper epidermis revealed the existence of unicellular and round or spherical shaped glandular trichomes that originated from both the upper and lower epidermis. A section through the central midrib revealed the alignment of round and thick-walled collenchymatous tissues. Beneath the collenchymatous layer exists the cortex, composed of ground tissues made up of round to oval shaped parenchymatous cells showing intercellular spaces. The central portion of the section is composed of a collateral vascular bundle with phloem arranged externally and xylem (exarch) radiating towards the centre. Phloem is represented by soft sieve elements, whereas xylem is represented by vessels, tracheids, fibers, and xylem parenchyma, all of which show strong lignification on their walls.

A transverse segment through the petiole (**Fig. 9C**) revealed a round to oval-shaped section covered with a single layer of epidermis, followed by 5-6 layers of collenchymatous tissues. Lignified unicellular trichomes with a bulbous base were seen originating from the epidermis (**Fig. 9D**). The cortex is made up of (a) round to oval parenchymatous cells with intercellular spaces and (b) a vascular bundle with collateral arrangements projecting towards the pith. The vascular bundle is made up of phloem tissues placed outwardly and xylem tissues organised inside. The xylem is distinctly endarch, and the walls are made up of lignin. There is a plainly visible pith in the centre, which is made up of large parenchymatous cells with intercellular spaces. In the pith, clusters of calcium oxalate crystals and starch grains were seen (**Fig. 9E**).

The histological section of the roots revealed the normal arrangement of the cork layer, composed of compressed striated cells (**Fig. 9F**). A layer of randomly arranged stone cells with lignified walls was seen interspersed in the cortex. The central region is composed mostly of

vascular bundles showing secondary growths and distributed randomly in the section. Uniseriate medullary rays were detected radiating towards the centre of the section. The xylem components were arranged endarch and showed deep lignifications of the walls.

The physicochemical constants of powdered plant sample were determined and summarised in **Table 2**. The determined concentrations of heavy metals like copper, arsenic, zinc, cadmium, mercury, and lead are summarised in **Table 3**. Results indicated that the estimated values were found to be within the limits prescribed by the WHO guidelines. Mycotoxin, aflatoxins B1, B2, G1, and G2, and total aflatoxin content are given in **Table 3**. The concentration of each of the above was found to be less than 1.0 µg/kg.

Table 1 Macroscopic characteristics of *N. herpeticum* leaf

Parameters	**Observations**
Colour	Green
Size	15-20 cm x 10-15 cm
Shape	Broadly ovate, cordate to truncate leaf
Taste	Characteristic
Surface characteristics	White hairs present
Texture	Roughly textured lamina

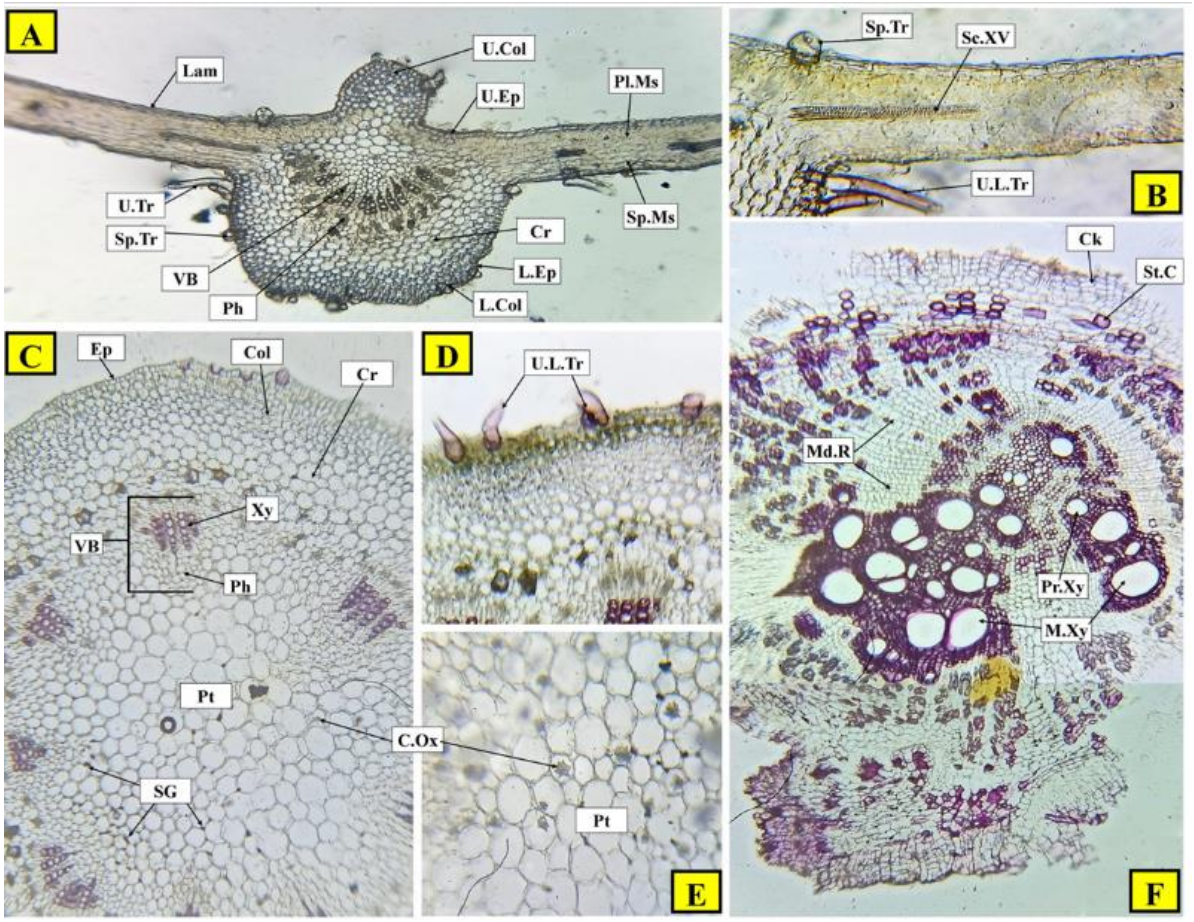

Fig. 9 Transverse section of the leaf (A-B), leaf petiole (C-E) and root (F) of *N. herpeticum*. Abbreviations: Lam-Lamina; U.Col- Upper Collenchyma; L.Col- Lower Collenchyma; U.Ep- Upper Epidermis; L.Ep- Lower Epidermis; Cr- Cortex; Pl.Ms- Palisade Mesophyll; Sp.Ms- Spongy Mesophyl; C.Ox- Calcium Oxalate Crystal; VB- Vascular Bundle; SP.Tr- Spherical Trichome; U.L.Tr- Unicellular Lignified trichome; Sc.XV- Xylem Vessel with Scalariform thickenings; Ep- Epidermis; Col: Collenchyma; Xy- Xylem; Ph- Phloem; SG- Starch grain; Pt- Pith; Ck- Cork; St.C- Stone Cells; Md.R- Medullar Rays; Pr.Xy- Protoxylem; M.Xy- Metaxylem

Table 2 Physicochemical parameters of *N. herpeticum*

Parameters	Results
Loss on drying	61.5460 ± 0.0161 (%w/w)
Total ash	25.1275 ± 0.0028 (%w/w)
Acid insoluble ash	0.7262 ± 0.0344 (%w/w)
Water soluble ash	24.1568 ± 0.0490 (%w/w)
Alcohol soluble extractive	2.46 ± 0.0057 (%w/w)
Water soluble extractive	7.4375 ± 0.0173 (%w/w)
Foaming index	Less than 100

Table 3 Heavy metals and aflatoxin content of *N. herpeticum*

Content		Concentration
Heavy metals	Copper	11.02[$]
	Arsenic	> 0.20[$]
	Zinc	45.72[$]
	Cadmium	> 0.20[$]
	Mercury	0.973[$]
	Lead	0.449[$]
Aflatoxins	Mycotoxin	Below quantification limit[#]
	Aflatoxin B_1	Below quantification limit[#]
	Aflatoxin B_2	Below quantification limit[#]
	Aflatoxin G_1	Below quantification limit[#]
	Aflatoxin G_2	Below quantification limit[#]
	Total aflatoxin	Below quantification limit[#]

$Concentration (in mg/kg), **#**Concentration (Lower Limit of Quantification 1.0 µg/kg)

5.3 Acute toxicity study

All test animals survived the 14 days of observation period post treatment with no behavioural changes. Both the control and test groups demonstrated weight gain by day 14, which indicated the normal growth of the animals (**Appendix (Supplementary Information): Table S1**). There were no significant changes in the relative organ weights and biochemical parameters, including total protein, albumin, globulin, alkaline phosphatase (ALP), aspartate transaminase (AST), and alanine transaminase (ALT), uric acid, urea, cholesterol, triglycerides, and creatinine (**Appendix: Table S2** and **S3**, respectively). Apart from this, there were no evident abnormal physical or clinical signs. Gross necropsy and histological assessment revealed no observable lesions in the organs, particularly the liver, lungs, heart, kidney, and ovary. Based on these findings, the LD_{50} of the extract was measured to be >5,000 mg/kg body weight.

5.4 Repeated dose 28-day oral toxicity study

Based on the results of the acute toxicity test, we chose dose ranges of 500, 1000, and 2000 mg/kg b.w. (groups named NH500, NH1000, and NH2000, respectively) for a 28-day toxicity study with repeated doses. No lethality was observed following oral administration of different concentrations of the extract in both female and male groups. All rats were found to be in good clinical health prior to and at the end of the study, and all rats exhibited no observable changes in skin, fur, eyes, or mucous membrane. No convulsions, salivation, or diarrhoea were observed. Nevertheless, lethargy was seen among both female rats on day 21 (n=2) and day 28 (n=4) and male rats on day 21 (n=3) and day 28 (n=3) in the high dose group.

Repeated administration of the extract (at all doses) in female animals showed a significant decrease in the % body weight gain as compared to the control group on day 21 and 28 (**Fig. 10A**). On the other hand, male animals receiving the extract doses exhibited reductions in % body weight gain from day 14 onward to day 28 (**Fig. 10B**). The male satellite group also

showed a significant decrease in percent body weight gain on day 14, 21, and 28. However, the satellite group of both female and male animals showed an increase in the percentage body weight gain at the end of the 14-day follow-up study (withdrawal of the dose).

The water intake of the female rats was seen to be significantly reduced in the high dose and satellite groups as compared to the control group on day 21 and 28. In males, the water intake was observed to be significantly reduced from day 14 onward to day 28 for the high-dose and satellite groups. The satellite group of both male and female groups showed a reversal of the decrease in water intake by day 14 of the follow-up study (**Fig. 11**). On the other hand, food intake in the females was significantly reduced ($P < 0.001$) in the high dose group (including the satellite group) from the 2^{nd} week until the 4^{th} week when compared to the control. The low dose group showed a significant reduction ($P < 0.01$) in food intake on day 28, while the medium dose group showed decreased food intake on day 21 ($P < 0.05$) and day 28 ($P < 0.001$). In comparison to the females, the male animals showed high variations in food intake, as represented by standard deviations. The 500 mg/kg group showed a significant reduction in food intake on the 28th day, whereas the medium dose group showed a significant reduction on day 21 and 28 compared to the control group. The high-dose and satellite groups showed a significant reduction in food intake by day 28 ($P <0.001$). Both male and female satellite groups showed a reversal of this decrease in food intake on the 14-day follow-up study (**Fig. 11**).

Necropsy study revealed no observable organ lesion and significant changes in the relative weight in both female and male animals (**SI: Table S4** and **S5**, respectively). Biochemical analysis revealed significant changes in high dose animals. In female animals, there was a significant change in globulin ($P <0.01$) and AST ($P <0.05$) levels in the medium dose group as compared to the control group. Similarly, there were significant changes from the normal range in all the measured biochemical parameters (except for albumin) in the female group receiving a 2000 mg/kg dose (**Table S6**). On the other hand, only the high-dose male group

showed significant changes in total protein ($P < 0.01$), ALP ($P < 0.001$), AST ($P < 0.05$), and ALT ($P < 0.01$) as compared to the control group (**Table S7**). In addition to this, no significant changes in any of the biochemical parameters of the satellite groups (both female and male) suggest this effect to be reversible on withdrawal of the dose.

H&E staining of heart, kidney, and lung tissues showed no significant changes in the histology in the low, medium, and high dose groups (**Fig. 12**). Examination of the hepatic sections in the control group (both male and female) revealed hepatic architecture with normal hepatocyte cords radiating from the central vein in a tightly packed fashion (**Fig. 12(D)**). Animals in the female group (n=2) receiving repeated high dose (2000 mg/kg) exposure showed some observable lesions in liver tissues. Liver sections of these two animals exhibited a slight dilatation of the blood sinusoids and a few cells of leukocytes, as shown in **Fig. 12(H)**. No severe damage or injuries were observed in the liver tissues. The satellite (female group) animals did not reveal any injuries, which suggested the liver injuries are reversible on dose withdrawal. However, low and medium dose groups (as well as high dose and satellite groups of males) showed no significant histopathological changes in both male and female animals.

Overall, the initial findings relevant to change in weight gain indicated a tendency towards the induction of toxicity in both males and females to a certain extent. Despite this, there were no notable physical abnormalities or behavioural patterns, except for a lethargic response in a few animals representing a loss of appetite. These findings are correlated with the increase in biochemical parameters in both the female and male groups to varying degrees. To mention, though these biochemical changes were statistically significant in difference from the control group, the values were within the lower and higher limits prescribed in previous literature [73]. We believe, these changes are due to the difference in methodologies employed.

Liver histology suggests that the repeated high dose exposure to the extract may potentially cause liver lesions in the animals. Two female animals displayed leukocyte infiltration and

sinusoids dilatation, which is consistent with the changes in biochemical parameters. This implies that repeated high dose administration may potentially cause liver injuries.

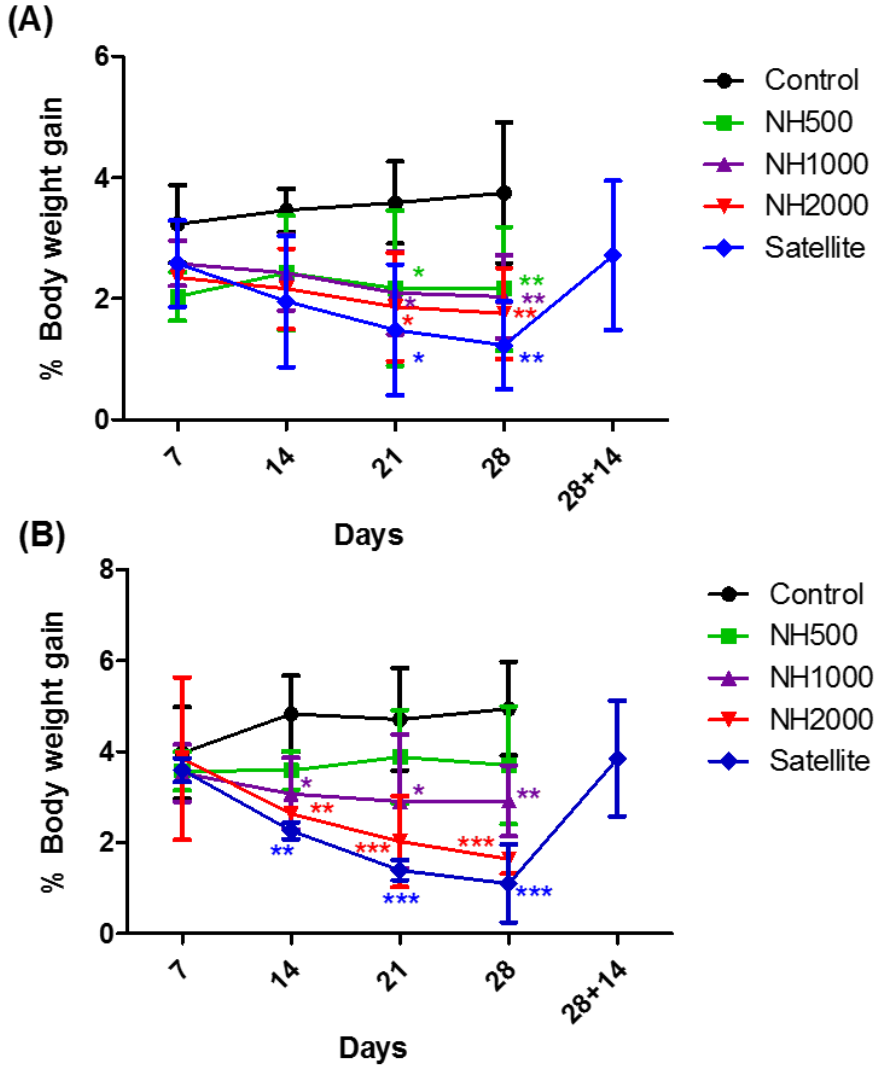

Fig. 10 % Body weight gain of female rats (A) and male rats (B) at different time point of measure. All values are Mean ± SD (n = 5). *P< 0.05, **P< 0.01, ***P< 0.001 compared to Control [Two-way ANOVA followed by Bonferroni test]

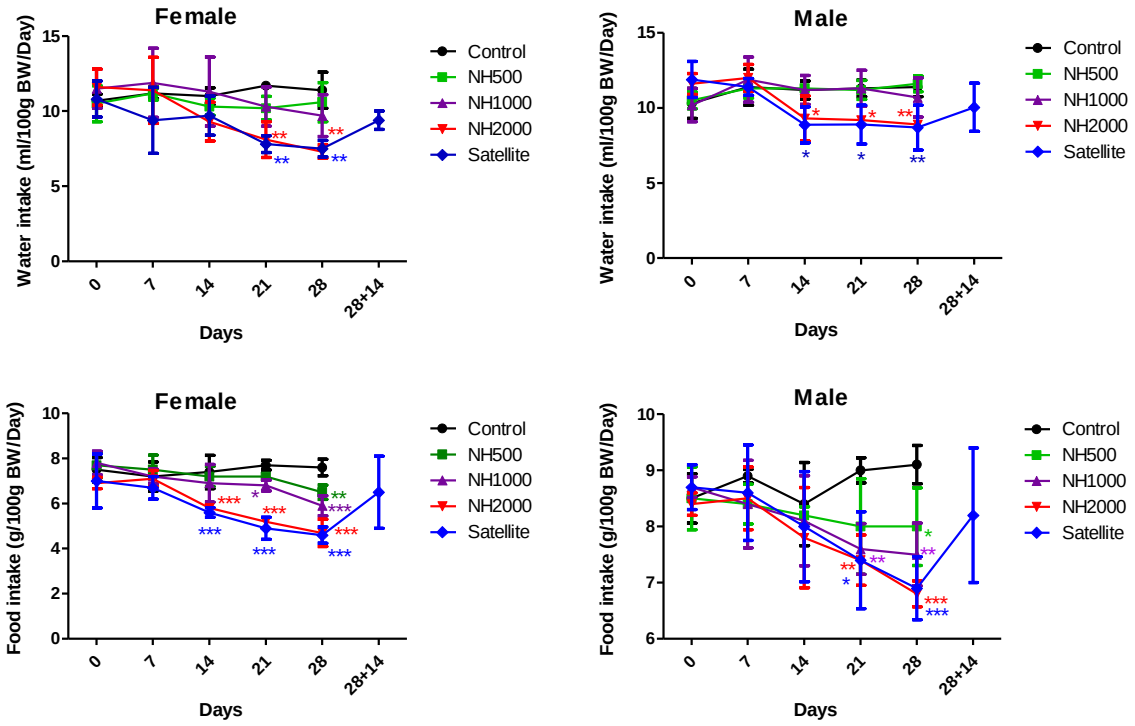

Fig. 11 Consumption of water (ml/100g body weight/ day) and food (g/100g body weight /day) of animals (male and female) at different time point of measure. All values are Mean ± SD (n = 5). *P< 0.05, **P< 0.01, ***P< 0.001 compared to Control [Two-way ANOVA followed by Bonferroni test]

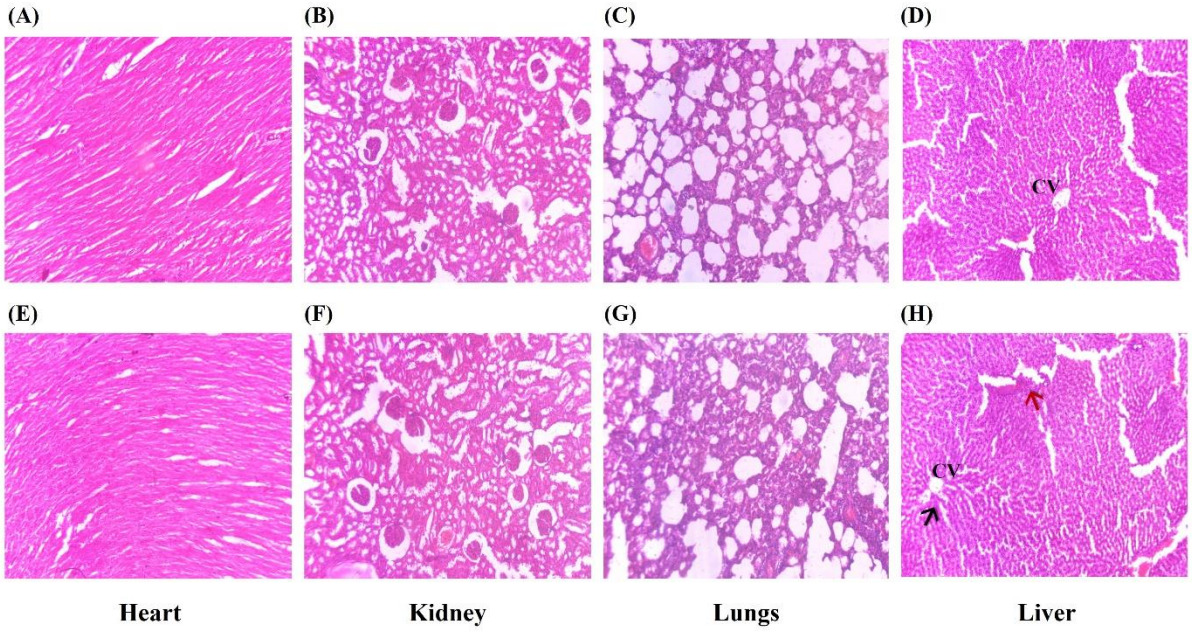

Fig. 12 Representative histopathological observations in female animals, i.e. control (A-D) vs. 2000 mg/kg dose (E-H), after repeated dose 28-day oral toxicity study. CV: Central vein; Black arrow: dilatation in blood sinusoids; and Red arrow: leukocyte infiltration (H&E staining 10X)

5.5 Qualitative analysis using LC-MS

QToF-MS profiling analysis revealed the presence of 21 representative compounds in the extract (**Table 4 and Table S8**). Comprehensive information from PubChem and the LOTUS database was retrieved about the LC-MS database-identified compounds. The LC-MS chromatogram and MS-spectra of positive and negative modes are shown in **Fig. 13, 14, and 15**, respectively. The drug-like molecules (14 out of 21), viz. HPA, HME, MLC, MOA, AZA, HTN, NMC, MMA, PPD, HHA, FLC, STG, AXT, and DPA, and their protein targets were traced out using SwissADME (**Table 4)** and the SwissTargetPrediction database (**SI: Table S9**). Four compounds (MLC, MMA, STG, and AXT) did not show any target genes. Upon removal of duplication, 329 potential targets were identified after eliminating the duplicate targets (**Fig. 16 and 17**).

Table 4 Representative compounds identified by QToF-MS and their drug-likeness properties

Abb.	Formula	RT	MW	HBA	HBD	MlogP	Lip. Vio.	BS
HPA	$C_9H_{18}O_3$	5.605	174.24	3	2	1.40	0	0.85
HME	$C_{18}H_{27}NO_3$	4.633	305.41	3	2	2.69	0	0.55
MLC	$C_{26}H_{33}NO_4$	8.288	423.54	4	3	2.69	0	0.55
MOA	$C_9H_{18}O_2$	9.278	158.24	2	1	2.28	0	0.85
COG	$C_{26}H_{28}O_{14}$	5.45	564.49	14	9	-3.56	3	0.17
AZA	$C_9H_{16}O_4$	6.606	188.22	4	2	1.25	0	0.85
HTN	$C_{28}H_{37}NO_9$	9.267	531.59	10	2	1.20	1	0.55
MAA	$C_{24}H_{41}N_{10}$	10.782	503.58	10	4	-0.96	2	0.17
LMS	$C_{18}H_{28}O_{11}$	11.584	420.41	11	6	-2.28	2	0.17
NMC	$C_{28}H_{47}NO_7$	13.86	509.68	8	1	1.57	1	0.55
MMA	$C_{31}H_{38}N_2O_7$	14.243	550.64	7	4	1.57	1	0.55
SPA	$C_{39}H_{56}O_{12}$	14.342	716.85	12	4	1.09	2	0.17
PPD	$C_{28}H_{44}O_5$	16.039	460.65	5	4	2.84	0	0.55
HHA	$C_{16}H_{32}O_3$	16.516	272.42	3	2	3.31	0	0.85
KKD	$C_{27}H_{44}O_{16}$	16.926	624.63	16	9	-3.65	3	0.17
FLC	$C_{25}H_{24}O_4$	17.161	388.46	4	1	3.31	0	0.55
APP	$C_{33}H_{40}N_2O_9$	17.261	608.68	10	1	1.75	2	0.17
KLD	$C_{40}H_{54}O_3$	17.486	582.85	3	2	1.75	2	0.17
STG	$C_{38}H_{48}N_4O_2$	18.327	592.81	4	2	4.13	1	0.55
AXT	$C_{40}H_{52}O_2$	19.901	564.84	2	2	4.13	1	0.55
DPA	$C_{32}H_{48}O_8$	19.989	560.72	8	4	1.85	1	0.55

*__Abb__.-Compound abbreviations, **RT**- Retention time in minutes, **HBA**- Hydrogen bond acceptor, **HBD**- Hydrogen bond donor; **MW**- Molecular weight, **BS**- Bioavailability score, **Lip. vio.**- Lipinski violation

(A)

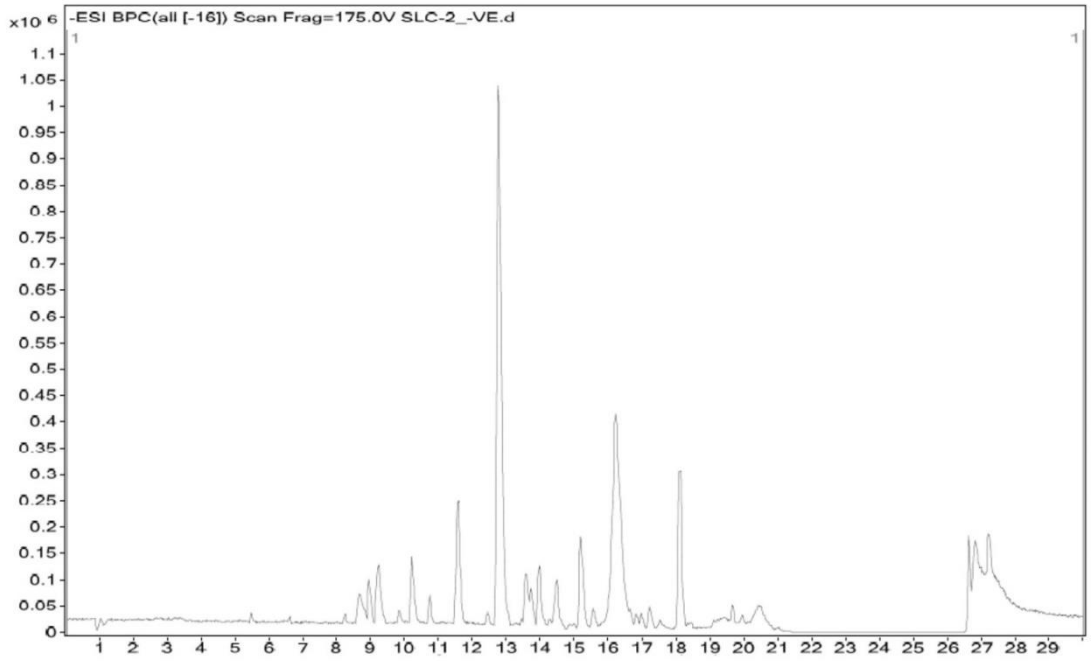

(B)

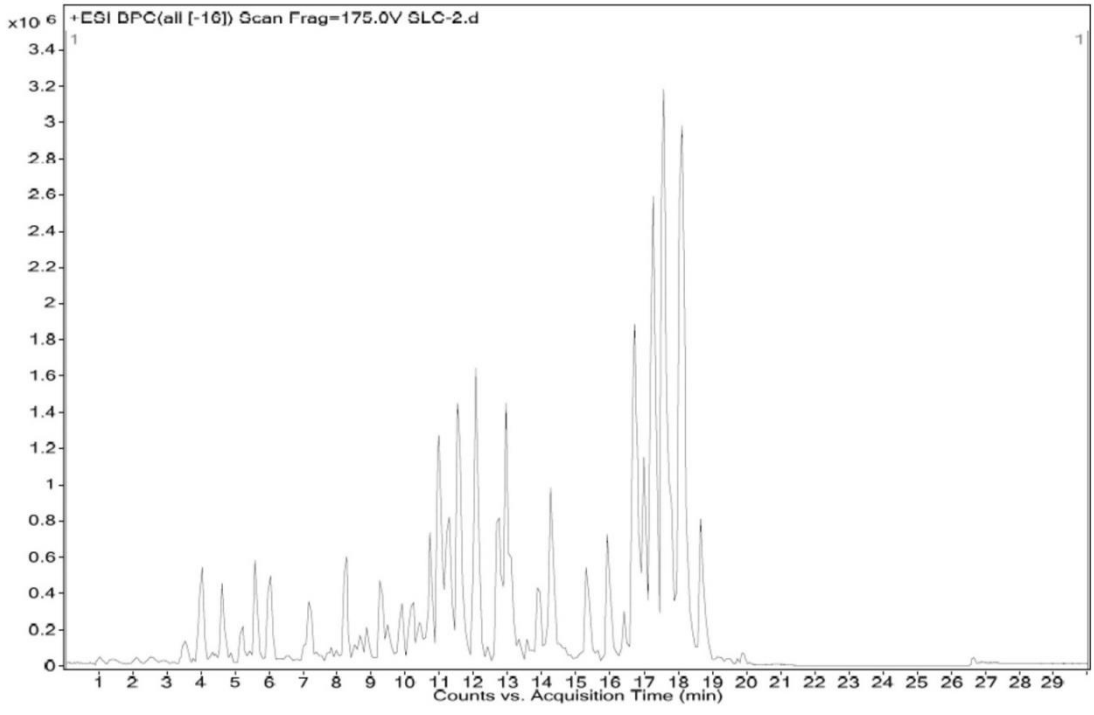

Fig. 13 LC-MS chromatograms of aqueous extract of *N. herpeticum*; (A) Negative mode, and (B) Positive mode

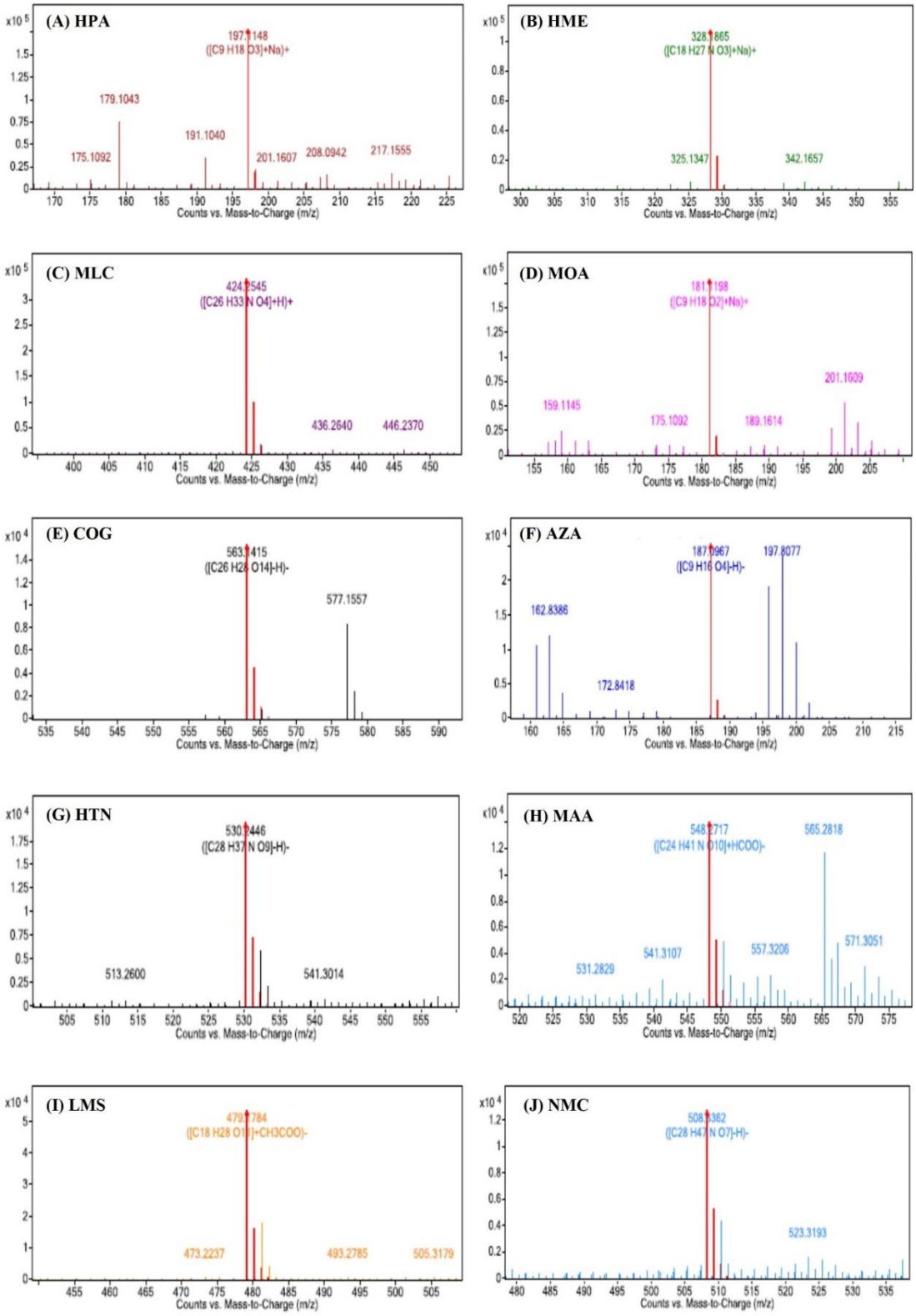

Fig. 14 MS-spectra of compounds detected in positive mode: (A) HPA, (B) HME, (C) MLC, and (D) MOA; and negative mode: (E) COG, (F) AZA, (G) HTN, (H) MAA, (I) LMS, and (J) NMC

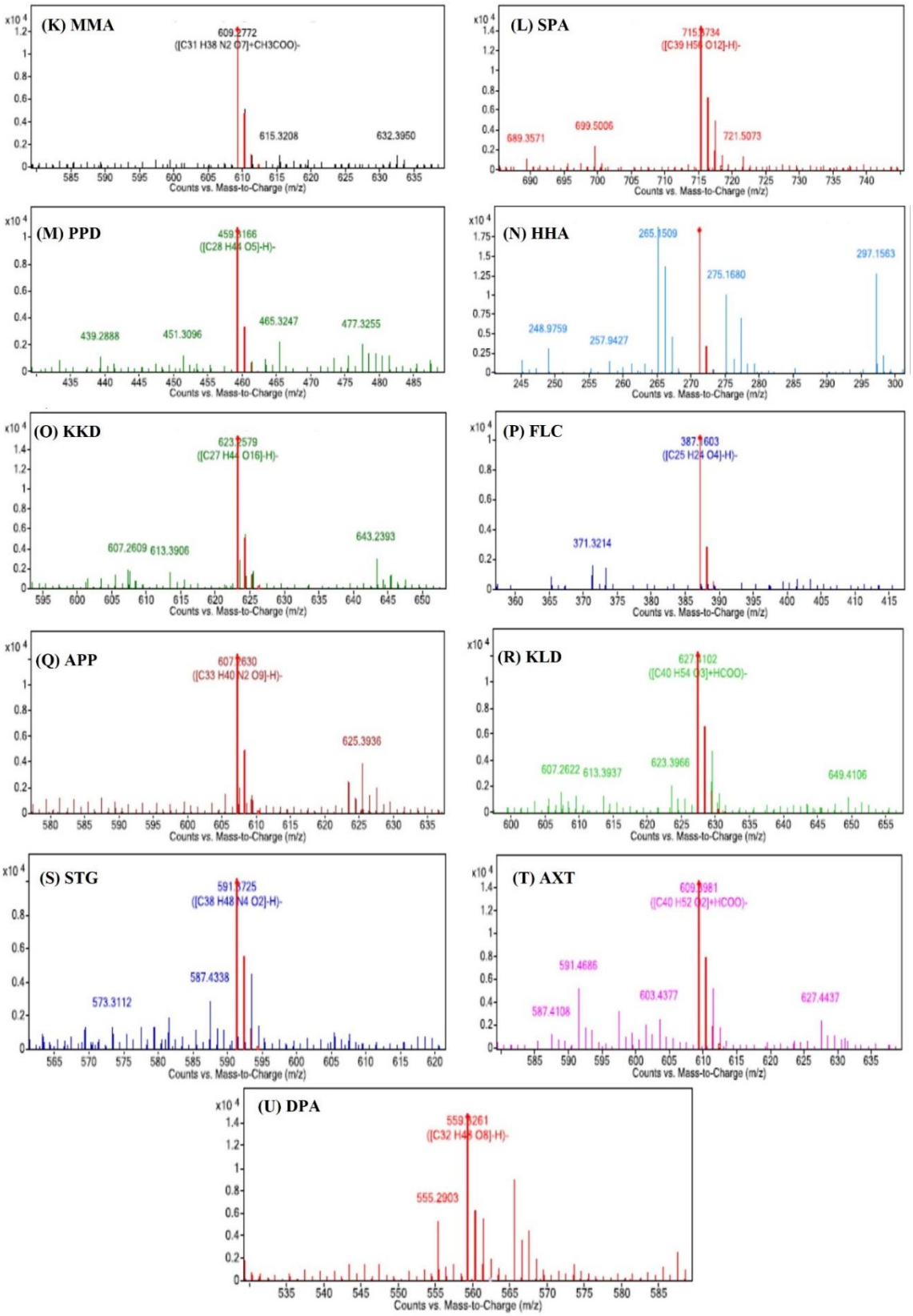

Fig. 15 MS-spectra of compounds detected in negative mode: (K) MMA, (L) SPA, (M) PPD, (N) HHA, (O) KKD, (P) FLC, (Q) APP, (R) KLD, (S) STG, (T) AXT, and (U) DPA

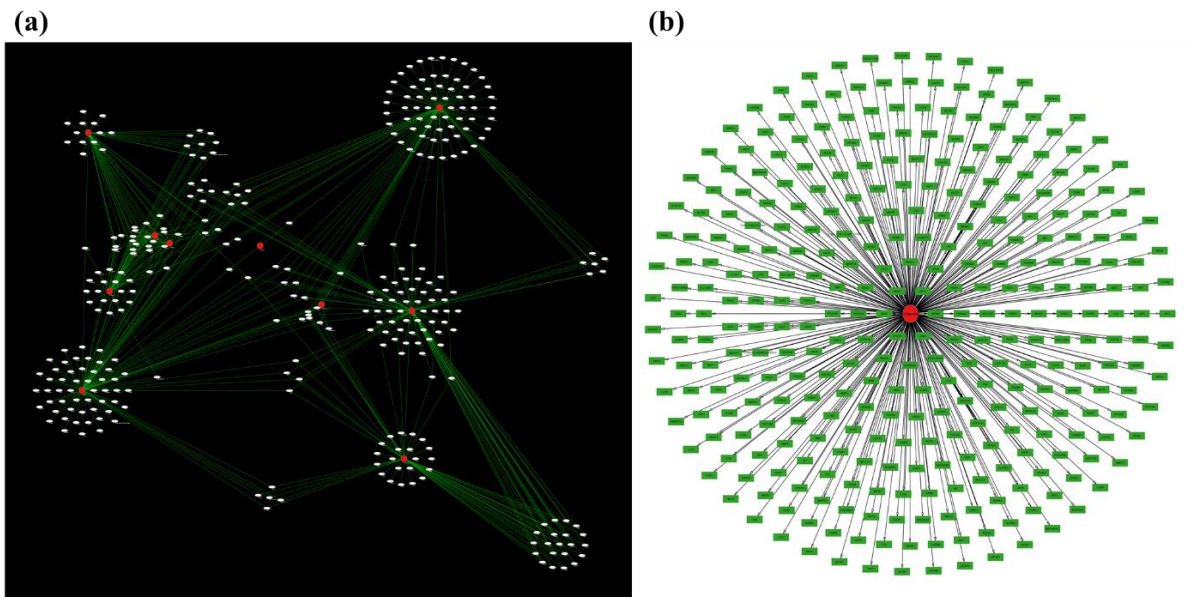

Fig. 16 (a) Network of identified targets for each of the compound. Red coloured ellipses represent compound, white boxes represent targets and green lines indicate their interaction **(b)** Total unique targets identified for the compounds after removal of duplication of targets. Red coloured ellipse represents compounds and green boxes represent targets

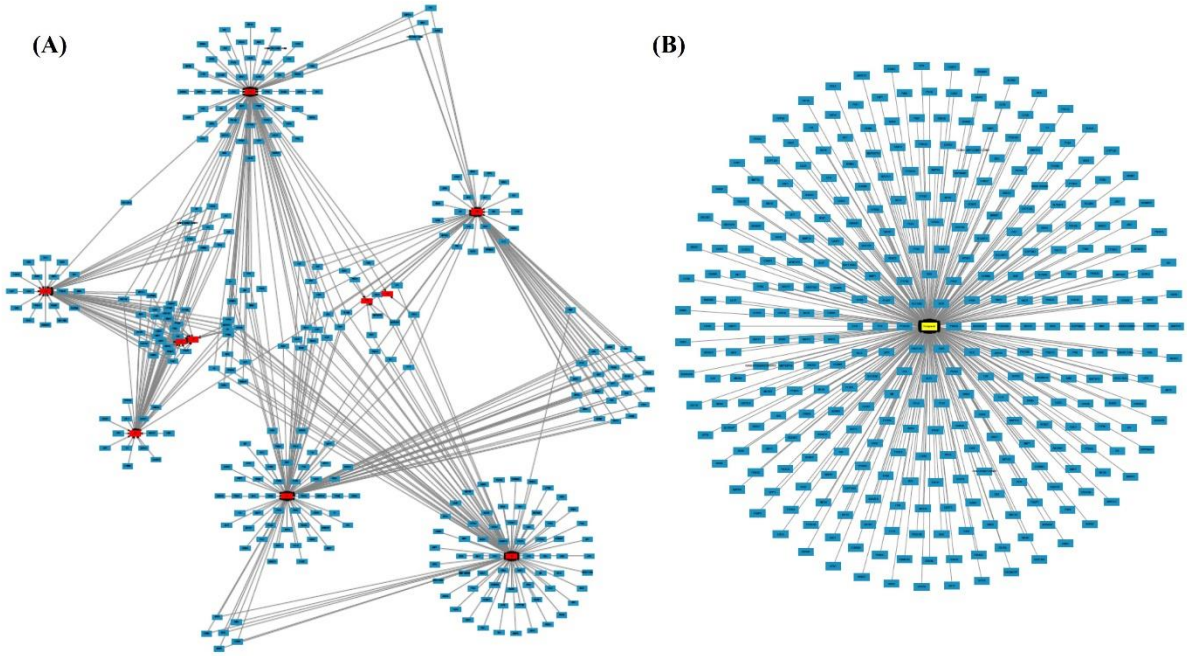

Fig. 17 (A) Compounds (probability score 0.1-1.0) and their target genes network. Red colour indicates compound and blue colour indicates target genes **(B)** Compound-target gene network after eliminating duplication of target genes. Blue colour indicates target genes and yellow colour indicates compound

5.6 Network Pharmacology Prediction

5.6.1 Antibacterial potential

An aggregate of 11914 and 15 targets were obtained from the GeneCard and DisGeNET databases, respectively. Upon removing the duplicate entries from the two, a total of 15 bacterial infection associated targets were found, as shown in **Fig. 18(a)**. MBL2, TNF, NOD1, IFNG, CRP, TBCE, SDC4, MYD88, IL6, CFTR, IRAK4, TLR4, IL1B, NOD2, and TLR2 were the identified targets **(SI: Table S10).** STRING analysis of these targets revealed a protein-protein interaction network with 15 nodes, 65 edges, an average local clustering coefficient of 0.833, and average node degree of 8.67. Characteristic path length (1.286), average number of neighbors (9.286), network radius (1), network diameter (2), network density (0.714), network heterogeneity (0.332), and network centralization (0.333) were calculated using the Cytoscape plug-in. The PPI enrichment p-value was <1.0e-16. Nodes and edges are representative of proteins and protein-protein associations in the network, respectively **(Fig. 18 (b) and 18 (c)).**

Using cytoHubba, calculations were done to rank the targets in the network based on betweenness centrality, closeness centrality, clustering coefficient, degree, and radiality. Other parameters like MCC, DMNC, MNC, EPC, bottleneck, eccentricity, and stress were also calculated to position the nodes in a constructed network. The network's topological parameters were the basis for ranking the targets in the network **(SI: Table S11 and S12)**. These targets might play an important role in the treatment of bacterial infections in *H. sapiens*, as they may be one of the potential key targets for the identified drug-like molecules in the aqueous extract. The bacterial infection-associated targets intersected with compound targets. An overlap of two targets was found, viz., interleukin-1 receptor-associated kinase 4 (IRAK4) and tumour necrosis factor (TNF) **(Fig. 18 (d)).**

STRING version 11.5 was accessed to construct a protein-protein interaction (PPI) network of two targets. The relationship between these targets in the PPI network was demonstrated and analysed based on KEGG enrichment (**SI: Table S13**). The KEGG analysis showed the involvement of TNF and IRAK4 in bacterial infections, including pathogenic *E. coli* infection, salmonella infection, tuberculosis, pertussis, and Yersinia infection. Apart from the bacterial infections, TNF and IRAK4 are also associated with leishmaniasis, herpes simplex virus type 1 infection, hepatitis B, influenza A, human immunodeficiency virus type 1 infection, chagas disease, and Epstein-Barr virus infection. Notably, network pharmacology analysis revealed the NF-κB signalling pathway (**Fig. 19**), the Toll-like receptor signalling pathway, the NOD-like receptor signalling pathway, and the MAPK signalling pathways as the identified pathways whereby the genes IRAK4 and TNF might target to modulate impaired cellular processes in host cells **(SI: Fig. S1)**. The cellular process modulations might be caused by mechanisms such as the induction of oxidative and nitrosative stress, activation of autophagy and apoptosis, and increased antigen processing and presentation, which in turn trigger necessary immune responses.

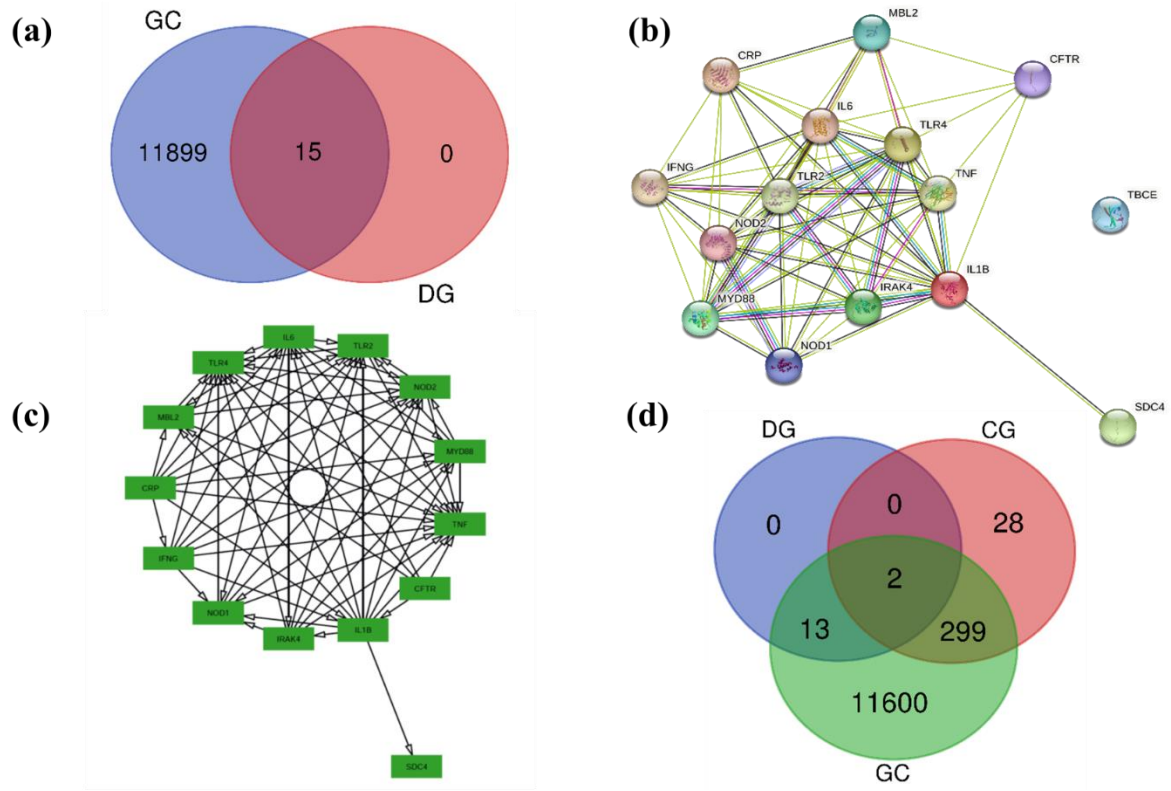

Fig. 18 (a) A Venn diagram showing the overlapping of GeneCard and DisGeNET database retrieved information about bacterial infection associated genes **(b)** STRING generated protein-protein interaction network of disease genes. Network nodes are represented as balls and edges as straight lines **(c)** Cytoscape generated protein-protein interaction network of disease genes. Green boxes represent the proteins and straight lines with arrow heads represent the interactions **(d)** A Venn diagram showing the overlapping of targets between DisGeNET, GeneCard and compounds. DG: DisGeNET; GC: GeneCard; CG: Compound genes

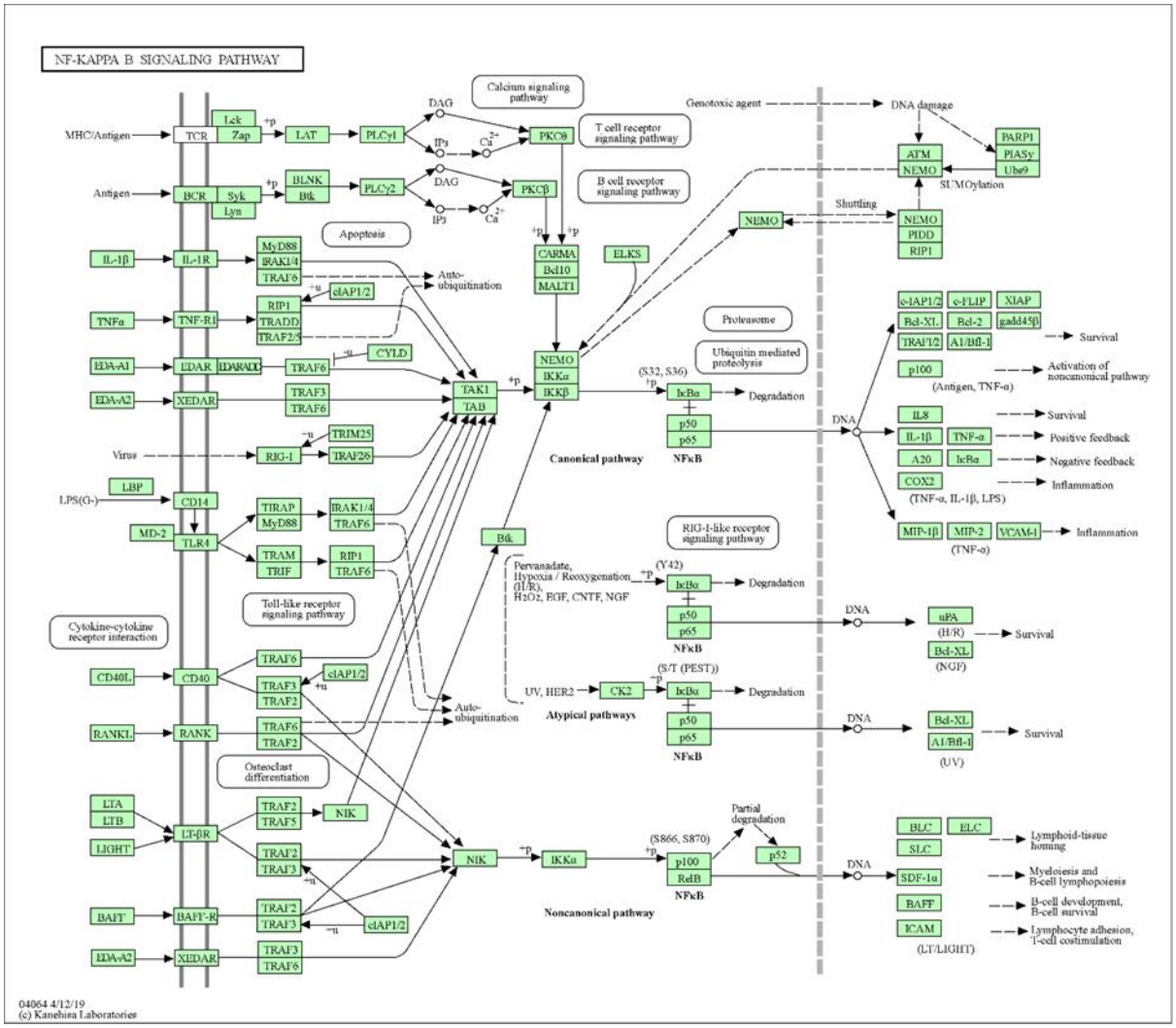

Fig. 19 KEGG Pathway- Genes associated with NF-κB signaling pathway

5.6.2 Anti-inflammatory potential

GeneCard and DisGeNET databases were opted for the retrieval of 11,274 and 175 targets relevant to inflammation, respectively. A Venn diagram showing a total of 174 targets in the intersection area is given in **Fig. 20 (A-B) and SI: Table S14**. A set of 27 targets was found to be common between compounds' targets and the genes linked with inflammation (**Fig. 21(A) and SI: Table S15**). With 27 nodes, 106 edges, an average node degree of 7.85, and an average local clustering coefficient of 0.684, the STRING-generated undirected PPI network (without clustering) of these targets was described (**Fig. 21(B)**). The PPI enrichment's p-value was 1.0e-

16, indicating that the network's interactions are significantly greater than what was anticipated. This demonstrates that there are more interactions between the proteins in the network than would be envisaged for a randomised group of proteins with the same size and degree of distribution taken from the genome. An enrichment of this kind suggests that the proteins are, at least partially, biologically connected. The PLAA gene was removed from the network as it exhibited zero-degree node interaction. The PPI network of the remaining 26 targets is shown in **Fig. 22(A)**. The number of nodes (26), edges (106), average number of neighbours (8.154), network diameter (3), radius (2), characteristic path length (1.705), network density (0.326), network heterogeneity (0.631), and network centralization (0.687) were all determined using Cytoscape. In the network, proteins are represented by nodes, whereas protein-protein relationships are represented by edges.

The topological properties of the STRING network were calculated (**SI: Table S16**). Topological analysis methods like Edge Percolated Component (EPC), Maximum Neighborhood Component (MNC), Density of Maximum Neighborhood Component (DMNC), Degree, Maximal Clique Centrality (MCC), clustering coefficient, and centralities (Bottleneck, EcCentricity, Closeness, Radiality, Betweenness, and Stress) based on shortest paths using Cytoscape were used to rank the targets in the constructed PPI network. Hub nodes in the PPI network were calculated based on closeness centrality, degree, and betweenness centrality. TNF, PTGS2, EGFR, STAT3, PPARG, PTGER4, PPARA, NOS2, TRPV1, and JAK2 are the top 10 nodes in the network (**Fig. 22(B)**). These targets showed greater interaction between hub nodes and nodes with potential control, as evident from their measures, viz., degree, closeness centrality, and betweenness centrality, respectively.

ShinyGO 0.77 was used for the analysis of functional enrichments in the network. The analysis was carried out by selecting an FDR cut off 0.05 and sorting by Fold Enrichment. GO-

biological process (**Fig. 23**), cellular component (**Fig. 24**), and molecular function (**Fig. 25)** enrichment analysis was carried out at p-value ≥ 0.5. The GO enrichment analysis encompassing target genes is shown in **SI: Fig. S2-S7**. The correlation between relevant pathways was summarised using plots and hierarchical clustering trees. Gene-sharing pathways tend to group together. Under similar operational settings, KEGG pathway enrichment analysis was done (**Fig. 26, SI: Fig. S8 and S9**). The top 10 ranked enriched KEGG pathways entailing target genes are shown in **SI: Fig. S10**. The adipocyte signalling pathway, PD-L1 expression, and PD-1 checkpoint in cancer, African trypanosomiasis, EGFR tyrosine kinase inhibitor resistance, arginine biosynthesis, alpha-linoleic acid metabolism, leishmaniasis, pancreatic cancer, ovarian steroidogenesis, and insulin resistance are the enriched KEGG pathways whereby the target genes exert action on the inflammatory condition associated with the pathways. The position of these target genes on human chromosomes is shown in **SI: Fig. S11**. In a nutshell, the enrichment analysis showed that target genes were involved in controlling a number of biological processes, molecular functions, cellular components, and the inflammatory pathways linked to a number of diseases.

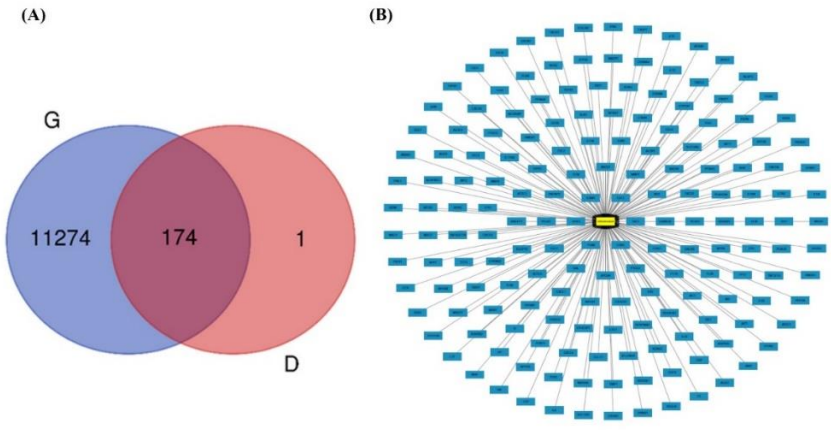

Fig. 20 (A) Venn diagram showing overlapping of inflammation-associated genes retrieved from DisGeNET and GeneCard databases. D: DisGeNet; G: GeneCard **(B)** Inflammation-gene network after removing duplication of genes. Yellow box indicates inflammation, and blue boxes indicate inflammation-associated genes

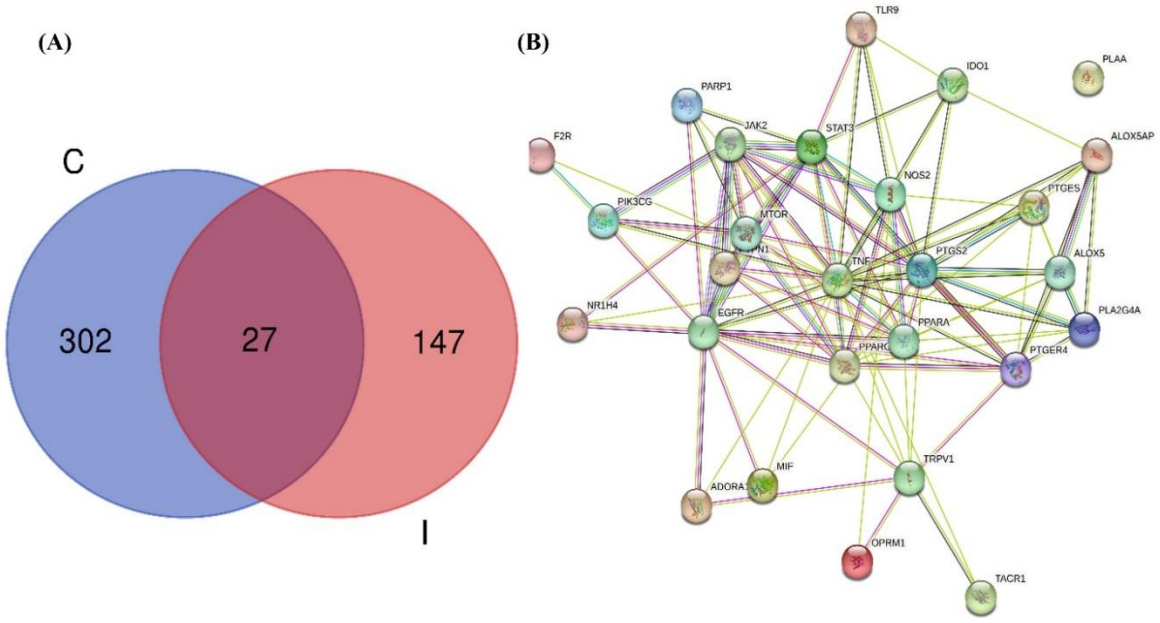

Fig. 21 (A) Venn diagram showing the overlapping of inflammation-associated genes with compound-target genes. C: Compound-target genes; I: Inflammation-associated genes, **(B)** STRING generated network of the 27 overlapping genes between inflammation-associated and compound-target genes. Nodes indicated as balls and edges as straight lines

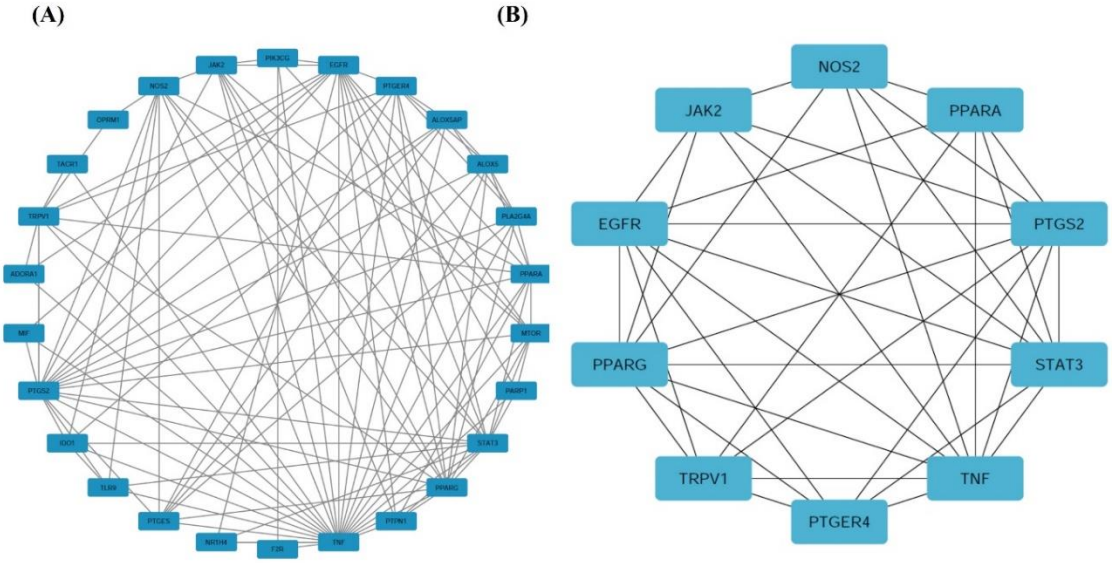

Fig. 22 (A) Cytoscape generated STRING network showing interaction of 26 overlapping genes between inflammation-associated and compound-target genes, **(B)** Sub-network showing interaction of top 10 nodes calculated based on degree. Blue coloured boxes indicate nodes (proteins) and grey coloured lines indicate edges (interactions)

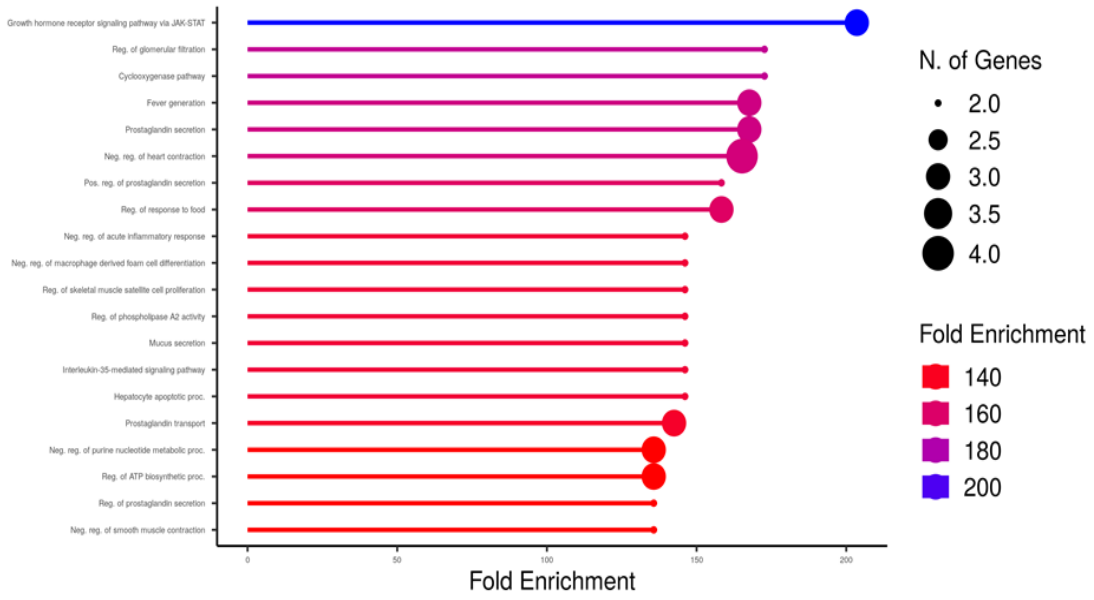

Fig. 23 GO-Biological process enrichment analysis using ShinyGO 0.77

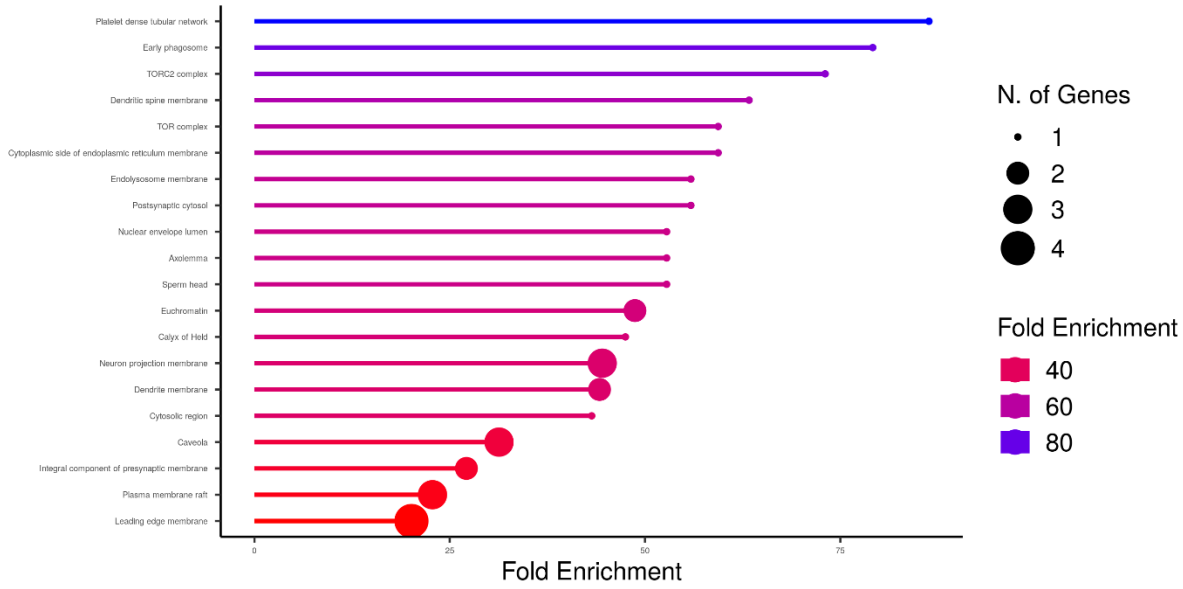

Fig. 24 GO-Cellular component enrichment analysis using ShinyGO 0.77

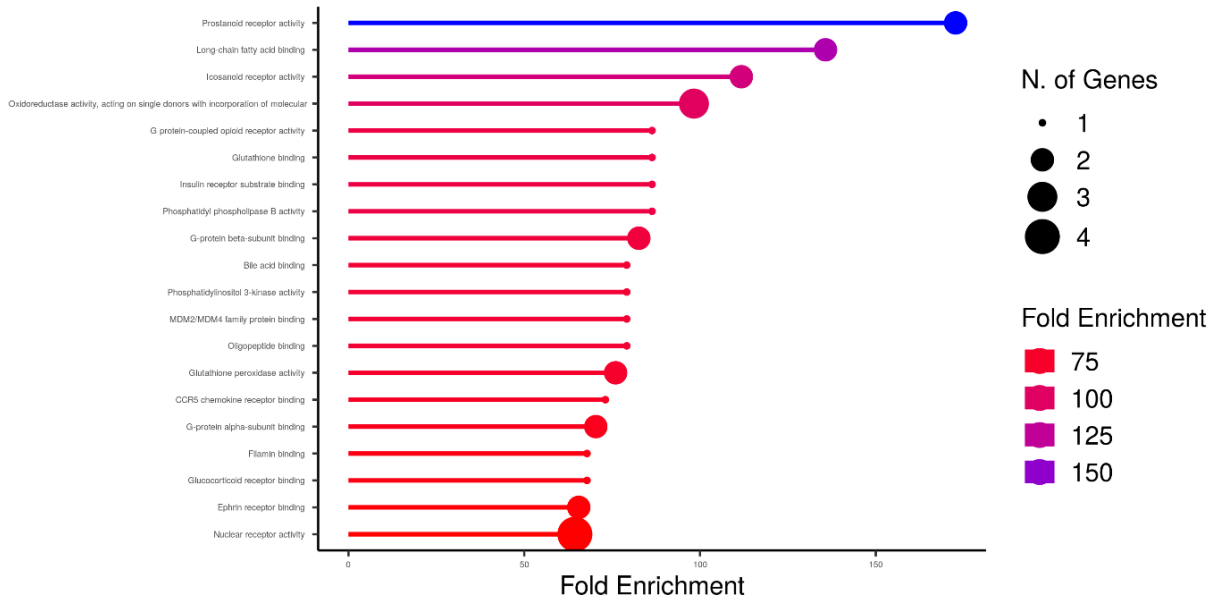

Fig. 25 GO- Molecular function enrichment analysis using ShinyGO 0.77

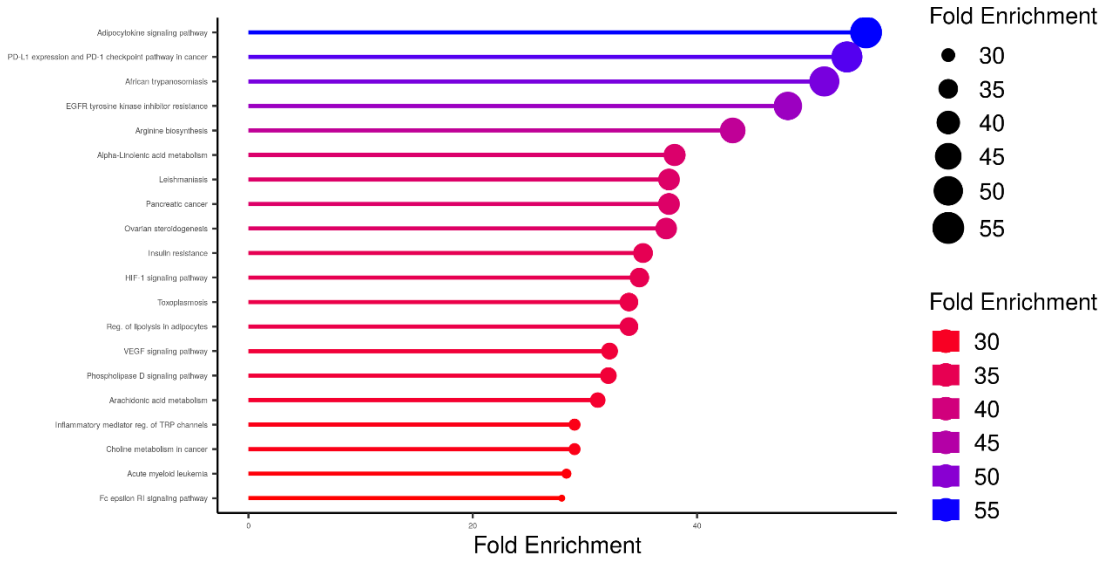

Fig. 26 KEGG pathway enrichment analysis using ShinyGO 0.77

5.7 In vitro antibacterial activity

In order to validate the in-silico results, we performed antibacterial assays using well diffusion and microtiter-plate dilution methods against *S. aureus*, *B. subtilis*, *E. coli*, and *P. aeruginosa*. In the well diffusion assay, after 24-hour incubation, the aqueous extract of *N. herpeticum* showed no zones of inhibition against the strains except for *E. coli* (zone of inhibition =

12.3±0.3 mm). However, positive control gentamicin (5 µg/ml) showed inhibition zones of 14.0±0.0, 22.0±00, 18.0±0.0, and 20.0±0.0 mm, respectively, against *S. aureus, B. subtilis, E. coli* and *P. aeruginosa*, representing the success of the well diffusion assay.

On the other hand, the aqueous extract of *N. herpeticum* exhibited potential antibacterial activity against *E. coli* and *P. aeruginosa* with an MIC of 50 µg/ml in microtiter-plate dilution assay (**Table 5**). However, the extract at all concentrations failed to inhibit Gram-positive bacteria in the microtiter-plate dilution assay, demonstrating a selective inhibition of Gram-negative bacteria. Furthermore, incubation of aliquots from the wells (with no visible growth) in sterile MHB revealed the activity of the extract to be bacteriostatic, as both *E. coli* and *P. aeruginosa* growth was evident for all the considered concentrations.

Table 5 Antibacterial activity of the aqueous extract of *N. herpeticum* against Gram-positive and Gram-negative strains

Strain	**Well-diffusion method**		**Microtiter-plate dilution method**			
	Aqueous extract of *N. herpeticum* (µg/ml)	**Positive control (µg/ml)**	**Aqueous extract of *N. herpeticum* (µg/ml)**		**Positive control (µg/ml)**	
	MIC	**MIC**	**MIC**	**MBC**	**MIC**	**MBC**
Staphylococcus aureus	NA	5	NA	ND	5	ND
Bacillus subtilis	NA	5	NA	ND	5	ND
Escherichia coli	100	5	50	NA	2.5	5
Pseudomonas aeruginosa	NA	5	50	NA	2.5	5

*Positive control: Gentamicin, ND: Not determined, NA: No activity

5.8 Molecular Docking studies

Initially, the docking protocol was validated by docking the co-crystallized ligand on the protein. The calculated Root Mean Square Deviation (RMSD) of the co-crystallized pose and redocked co-crystallized pose of the ligands are depicted in **Table 6 & Fig. 27**. Among the selected proteins, glucosamine-6-phosphate synthase (PDB: 2VF5) was an apoprotein. Hence, to determine the plausible binding site, we employed the site mapping protocol (refer to **Table 6** for xyz coordinates). Of the identified sites, an energetically favourable site was chosen for further studies. The docking results of the ligands against the four antibacterial targets are presented as docking scores of the ligands as Kcal/mol in **Table 7**. As the results indicate, compound HME showed the most promising profile against all four targets. Docking scores for HME against DNA gyrase subunit b (PDB: 1KZN), glucosamine-6-phosphate synthase (PDB: 2VF5), dihydrofolate reductase (DHFR, PDB: 2W9S), and penicillin-binding protein or PBP (PDB: 4CJN) were -4.75, -7.53, -6.15, and -5.01, respectively. All other compounds also showed satisfactory results but were found to possess less binding affinity as compared to HME. Thus, the binding interactions of HME were further analysed to understand the binding pattern at the binding site of each target.

Table 6 RMSD calculations of co-crystallized ligands and co-ordinates of the grid of proteins

PDB	**Co-ordinates of the grid**	**RMSD (Å)**
1KZN	X:-17.33, Y:11.20, Z:27.08	0.20
2VF5	X:-17.33, Y:13.20, Z:25.08	0.59
2W9S	X:-14.33, Y:11.20, Z:27.08	0.11
4CJN	X:-15.33, Y:15.20, Z:26.08	0.63

Table 7 Docking scores on four different receptors

Compounds	Docking scores (Kcal/mol)			
	1KZN	**2VF5**	**2W9S**	**4CJN**
HPA	-4.22	-4.70	-4.12	-4.60
HME	-4.75	-7.53	-6.15	-5.01
MLC	-2.81	-5.03	-4.82	-3.29
MOA	-3.18	-4.14	-4.09	-4.03
AZA	-1.56	-3.11	-3.04	-3.65
HTN	-3.84	-4.36	-2.77	-4.87
NMC	-5.36	-2.69	-3.07	-1.84
MMA	-2.70	-2.05	-3.73	-2.87
PPD	-4.39	-4.43	-4.30	-4.30
HHA	-3.75	-2.83	-5.42	-2.66
FLC	-2.66	-	-6.04	-3.11
STG	-4.07	-1.34	-1.88	-3.97
AXT	-	-	-	-
DPA	-3.52	-7.41	-2.98	-6.65
Kanamycin	-5.42	-13.11	-7.76	-8.43
Gentamicin	-6.13	-11.12	-6.89	-7.54

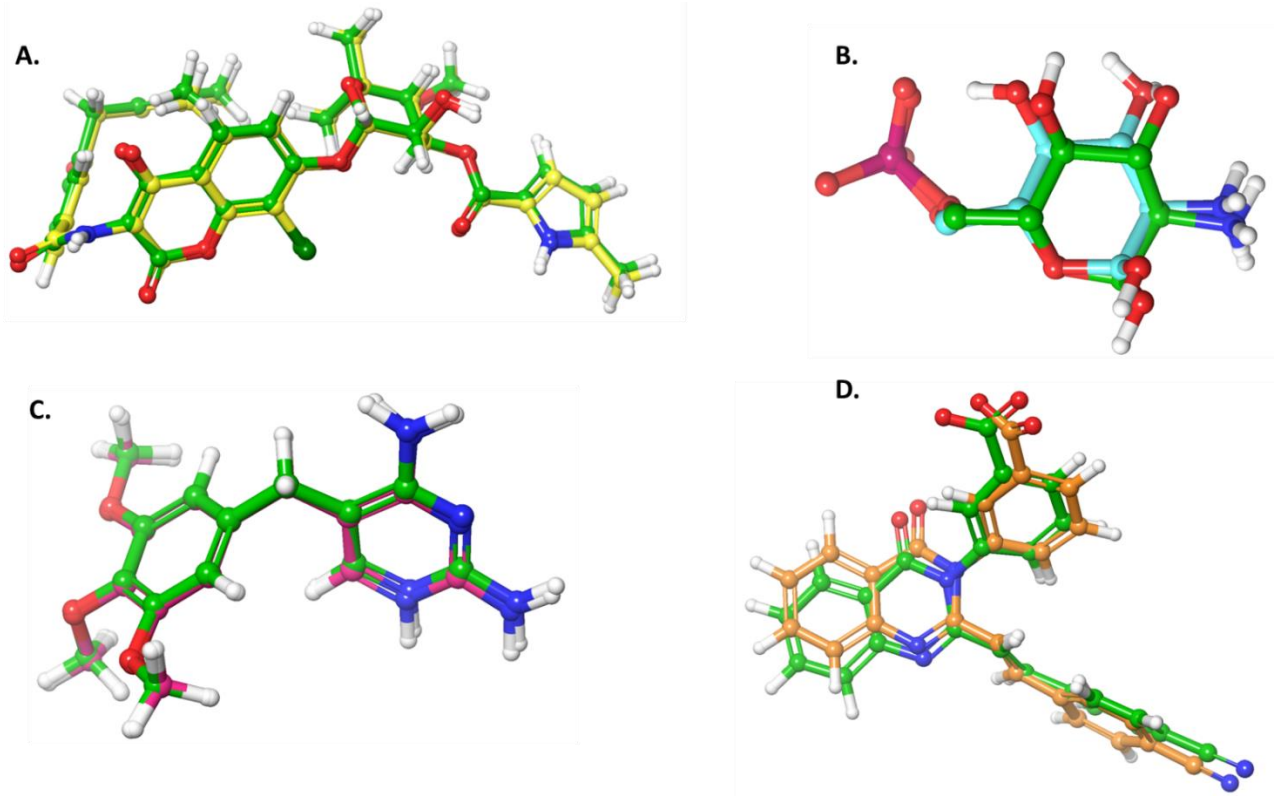

Fig. 27 (A) DNA gyrase subunit b (PDB: 1KZN) Co-crystallized ligand green colour and the redocked pose in green colour (B) Glucosamine-6-phosphate synthase (PDB: 2VF5) Co-crystallized ligand Cyan colour and the redocked pose in green colour (C) Dihydrofolate reductase (DHFR, PDB: 2W9S) Co-crystallized ligand green colour and the redocked pose in pink colour and (D) penicillin-binding protein (PDB: 4CJN) Co-crystallized ligand green colour and the redocked pose in orange colour.

At the active site of DNA gyrase subunit b (PDB: 1KZN), HME forms two hydrogen bonds. The hydroxyl functional group present at the benzene forms an H-bond with the Asp73 amino acid residue, while the secondary amino group (amide group) forms an H-bond with the Asn46 residue of DNA gyrase subunit b. HME binds to the active site of the enzyme, surrounded by hydrophobic amino acid residues Val167, Met166, Val120, Met91, Ile90, Pro79, Ile78, Ala47, and Val43, along with hydrophilic residues Asn46, Gln72, and Thr165 amino acid residues **(Fig. 28(a) and 28(b)).**

Docking against glucosamine-6-phosphate synthase (PDB: 2VF5), HME was surrounded by mostly hydrophilic residues, such as Thr302, Ser303, Ser347, Gln348, Ser349, Thr352, Ser401, Thr355, and Ser604. The carbonyl functional group of the amide linkage acts as an H-bond acceptor. It formed a bond with the Thr302 amino acid residue. In contrast, the hydrogen atom of the methoxy group (present at the benzene ring) acted as a hydrogen bond acceptor with the Ser303 amino acid residue of the enzyme. The hydroxy group is portrayed as an H-bond donor and is found to form two hydrogen bonds with amino acid residues Ser347 and Ser349 **(Fig. 28(c) and 28(d)).**

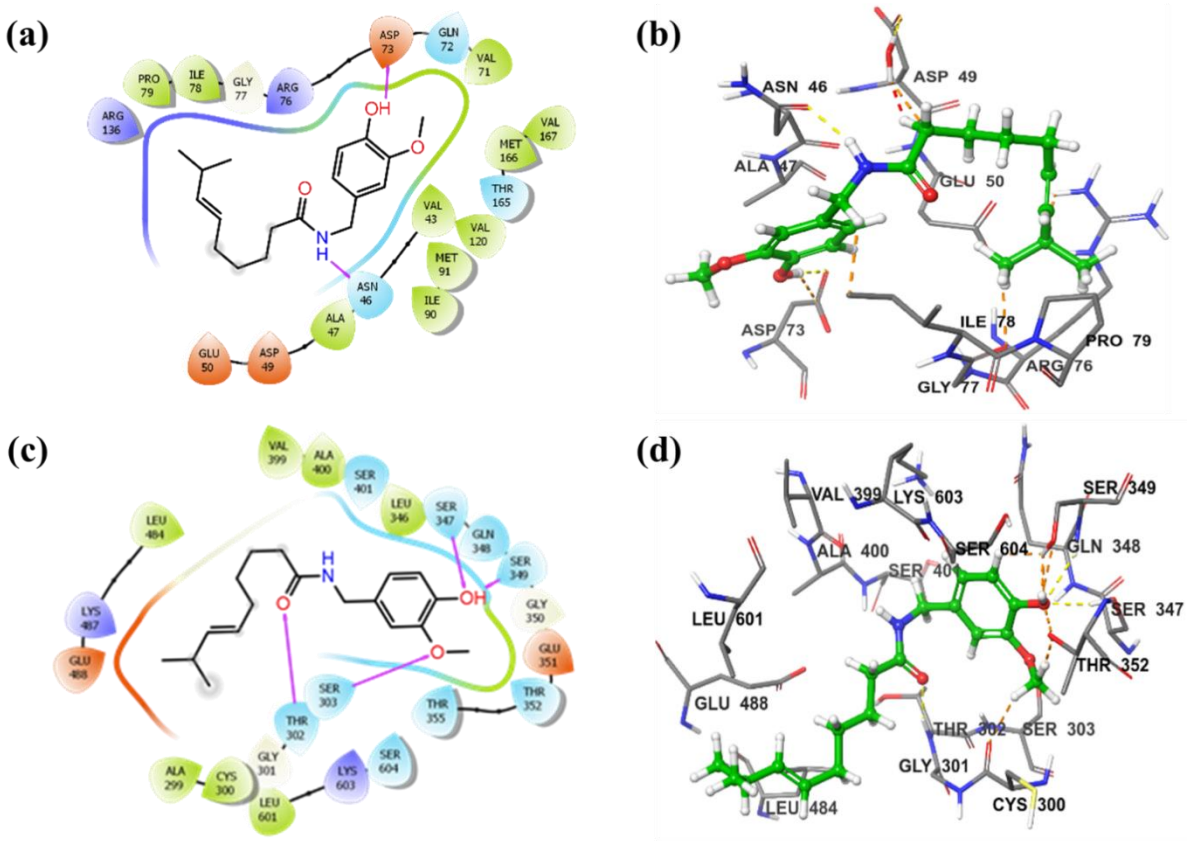

Fig. 28 (a) 2D docking interaction diagram of HME-1KZN **(b)** 3D docking interaction diagram of HME-1KZN **(c)** 2D docking interaction diagram of HME-2VF5 and **(d)** 3D docking interaction diagram of HME-2VF5

The ligand binding site of DHFR (PDB: 2W9S) is mostly lined by hydrophobic amino acid residues such as Ile5, Val6, Ala7, Leu20, Trp22, Leu28, Ile31, Ile50, Leu54, Pro55, Phe95, and Tyr98. The compound fits well between these residues. The carbonyl moiety of the amide linkage forms an H-bond with the water molecule present at the DHFR active site. At the DHFR enzyme active site, the hydroxyl group forms a hydrogen bond with the Asp27 amino acid residue **(Fig. 29(a) and 29(b)).**

In the same way, compound HME showed two hydrogen bond interactions with the PBP (PDB: 4CJN) when it was docked against it. The hydroxyl group demonstrated a hydrogen bond with the Glu239 residue and the carbonyl group with the Arg241 residue of the protein **(Fig. 29(c) and 29(d))**. Further, all compounds were subjected to a free binding energy calculation, where the compound HME showed the highest ΔG binding energy of -37.7 Kcal/mol among all the compounds. Thus, a correlation between the MM-GBSA calculations and the docking score was established (as depicted in **Table 8**).

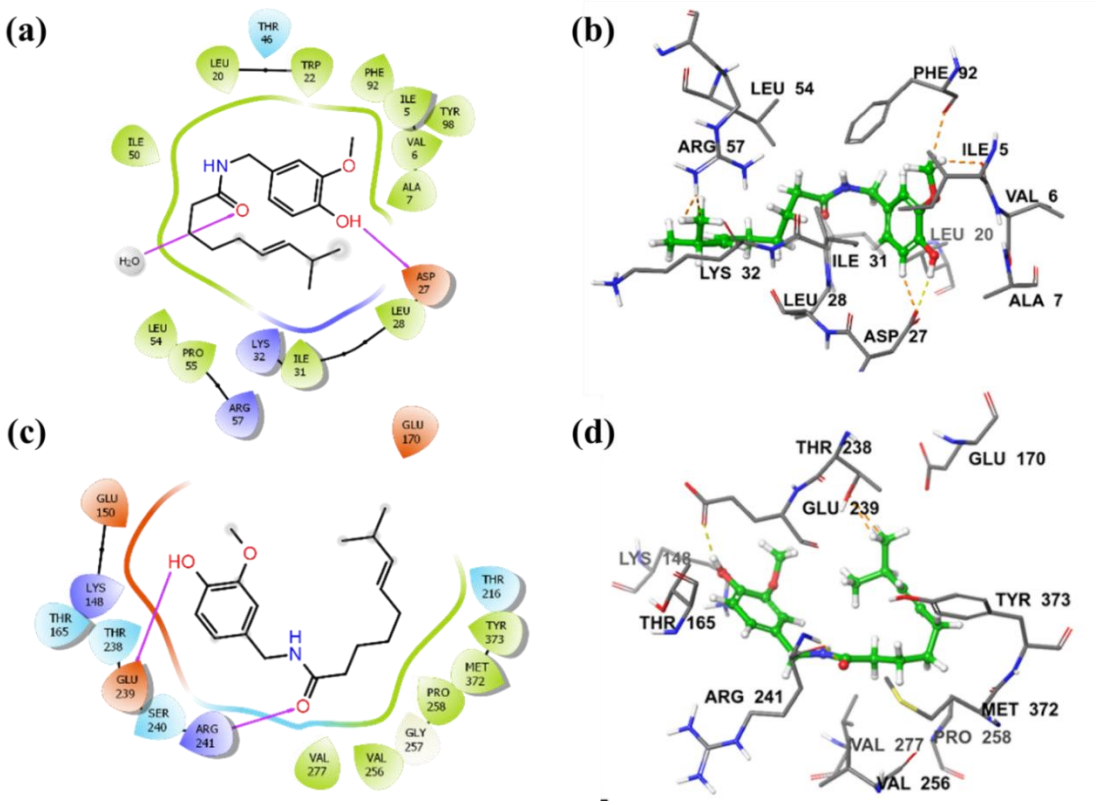

Fig. 29 (a) 2D docking interaction diagram of HME-2W9S **(b)** 3D docking interaction diagram of HME-2W9S **(c)** 2D docking interaction diagram of HME-4CJN and **(d)** 3D docking interaction diagram of HME-4CJN

Table 8 Output of MMGBSA Analysis on selected compounds on PDB ID: 4CJN

Compound	MMGBSA_dG_Bind	MMGBSA_dG_Bind_Coulomb	MMGBSA_dG_Bind_Covalent	MMGBSA_dG_Bind_Hbond	MMGBSA_dG_Bind_Lipo	MMGBSA_dG_Bind_vdW
HPA	-36.1107	-11.6959	10.54792	0.156763	-15.2193	-45.3839
HME	-37.786	0.499633	2.28088	-0.51009	-16.3351	-40.8942
MLC	-28.9763	-18.4421	3.047337	-0.99393	-7.60099	-32.979
MOA	-26.409	-11.8888	1.942177	-1.75337	-8.05228	-32.2007
AZA	-19.4012	-5.79023	-7.39181	-2.04711	-13.9647	-36.6624
HTN	-25.4271	-10.4225	4.731052	-0.90071	-11.7225	-34.1624
NMC	-37.8875	-10.2794	3.247885	-0.37659	-14.5061	-40.2088
MMA	-25.089	-3.18824	2.742902	-1.30625	-11.7588	-33.1141
PPD	-24.8437	-2.91909	1.533799	-0.7793	-10.6408	-29.3069
HHA	-24.6718	-9.05947	1.814279	-0.36848	-6.42466	-22.9688
FLC	-30.1717	-7.71283	0.552939	-0.36546	-11.8954	-29.7816
STG	-27.2616	-7.97861	9.516464	-0.93221	-14.9439	-44.7056
AXT	-	-	-	-	-	-
DPA	-21.3287	-6.88503	4.477068	-0.72767	-10.8698	-28.1134
Kanamycin	-20.8752	-1.21835	2.132966	-0.32304	-6.53403	-29.9628
Gentamicin	-38.4883	-5.32448	0.755375	-21.3498	-27.9156	-41.1743

5.9 Molecular Dynamic simulation study

The results from the MD trajectory analysis of the complex are shown in **Fig. 30** (for gentamicin) and **Fig. 31** (for HME). The protein-ligand complex (PL complex) RMSD plot of reference gentamicin (**Fig. 30(A)**) was found to be stable around 1.6-7.5 nm for over 40 ns. However, a slight fluctuation (but within the range) was observed in the 40-50 ns time period. On the other hand, for the PL complex of HME, the RMSD value was found to be within the adequate range, i.e., 1-3Å during the whole duration of simulation (**Fig. 31(A)**), indicating better ligand-protein complex stability in comparison with gentamicin. In order to anticipate the dynamic actions of the amino acid residues throughout the simulation and to find out the stability and flexibility of the protein, the root mean square fluctuation (RMSF) plot was examined. The results showed no internal fluctuations over the simulation period. The protein's RMSF value (both for gentamicin and HME; **Fig 30(B)** and **Fig 31(B)**) was found to be within the satisfactory range of 1.00 to 1.75 and 1.25 to 1.75 nm, respectively. The ligand's RMSF value was found to be in the range of 0.7-1.9 nm for gentamicin (**Fig 30(C)**), whereas it was at a proximity of 0.8-1.5 nm for HME (as depicted in **Fig. 31(C))** indicating a slight ligand fluctuation but firm catalytic pocket binding throughout the simulation of 50 ns. On evaluating the degree of P-L contacts in the case of gentamicin, the H-bond predominated the stability of the complex (**Fig 30(D)**). Amino acid residue GLU 481, followed by GLN 581, THR 577, and SER 401, were predominately involved in the H-bond interaction. The second major interaction that favoured the stability of the complex was the formation of water bridges. Also, amino acid residues GLU 481, followed by THR 302 and THR 406, were involved in the interaction. In the case of HME (**Fig 31(D)**), the hydrophobic interaction was found to predominate in the stability of the complex. The important amino acids that were involved in the interaction were ALA 584, ILE 489, PHE 405, and LEU 580. The next major interaction was the formation of

water bridges, mediated by VAL 595, followed by SER 401. H-bond was of negligible extent (SER 401) in the case of HME within the active protein domain.

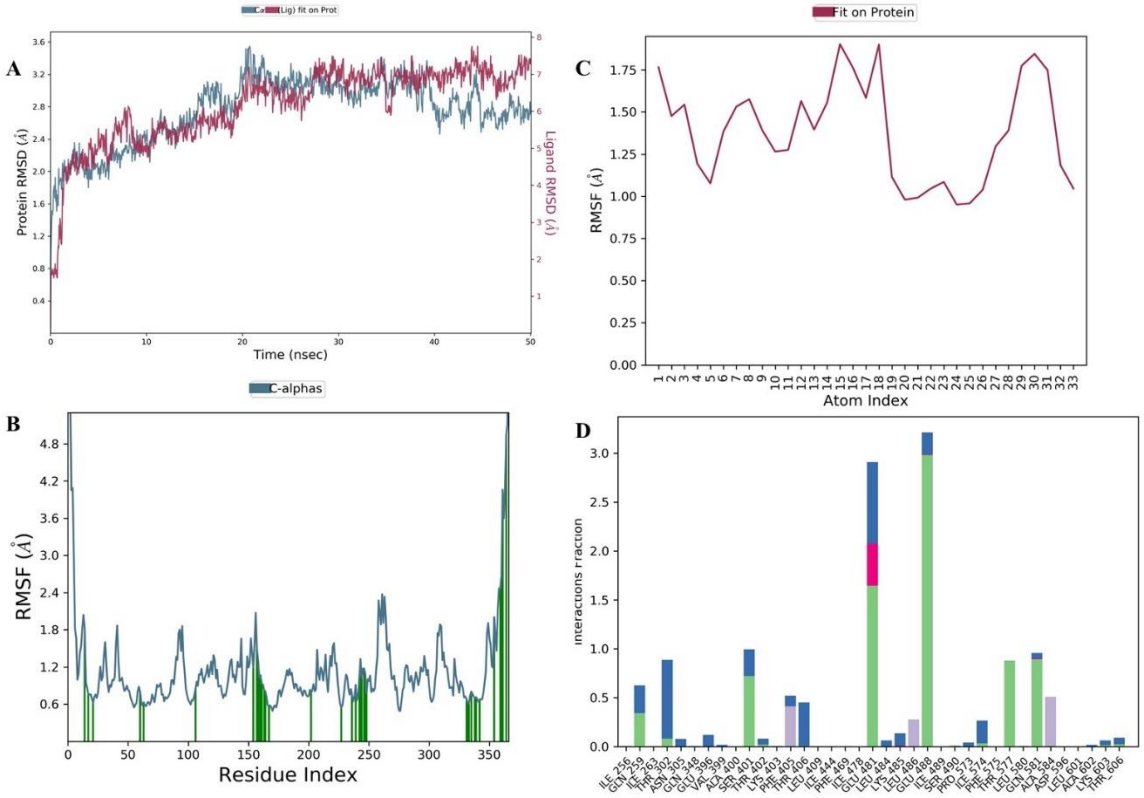

Fig. 30 Molecular dynamics trajectory analysis of the gentamicin-protein complex **(A)** Protein-ligand RMSD **(B)** Protein RMSF **(C)** RMSF for ligand, and **(D)** P-L Contact analysis

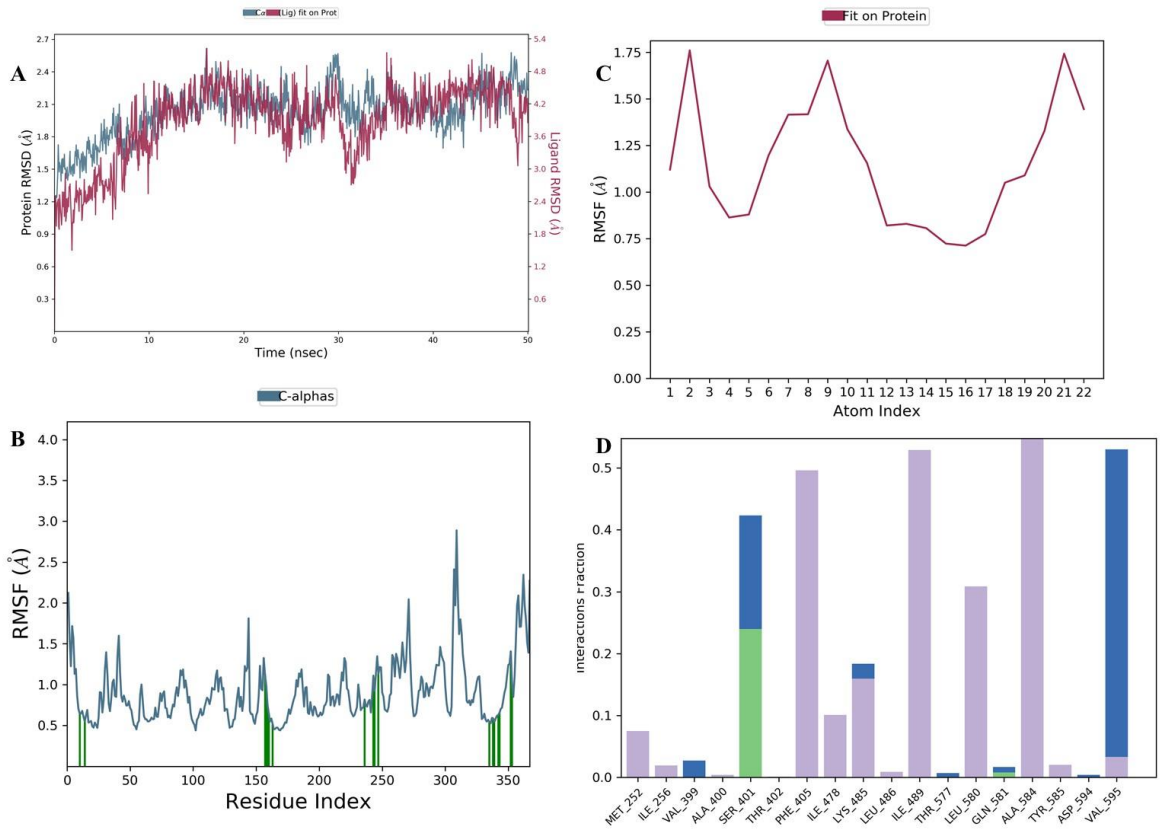

Fig. 31 Molecular dynamics trajectory analysis of the HME-protein complex (A) Protein-ligand RMSD (B) Protein RMSF (C) RMSF for ligand and (D) P-L Contact analysis

5.10 In vitro anti-inflammatory activity

In the protein denaturation assay, the aqueous extract of *N. herpeticum* demonstrated concentration-dependent inhibition of protein denaturation, as shown in **Table 9**. The percentage inhibition of protein denaturation by the extract was found to be within the range of 18.31±0.05 to 55.53±0.10% at the concentration range of 20-100 µg/ml. The IC_{50} value was determined to be 98.76 µg/ml (IC_{50} of control was 75.64 µg/ml). Similarly, in the proteinase inhibition assay, the extract showed percentage inhibition in the range of 23.50±0.58 to 60.89±0.71%, when compared to the control (23.32±0.77 to 66.61±0.20) (**Table 9)**. The IC_{50} value of the extract was found to be 85.73 µg/ml compared to 76.72 µg/ml of control. The

inhibitory effect of the extract on heat-induced haemolysis of RBCs is demonstrated in **Table 9**. A concentration of 96.16 µg/ml was determined to be the IC_{50} value of the extract, where 100 µg/ml demonstrated the highest amount of inhibition (53.61±1.05%). IC_{50} of aspirin (control) is 63.98 µg/ml. Overall, these results suggest that an aqueous extract of *N. herpeticum* possesses good in vitro anti-inflammatory activity when compared to the control aspirin within the considered range.

Table 9 In vitro anti-inflammatory activity of the aqueous extract of *N. herpeticum*

Concentration (µg/ml)	**Protein denaturation assay (% inhibition of protein denaturation)**		**Proteinase inhibition assay (% inhibition of proteinase)**		**Membrane stability assay (% haemolysis inhibition)**	
	Control	**Extract**	**Control**	**Extract**	**Control**	**Extract**
20	22.75±1.10	18.31±0.05	23.32±0.77	23.50±0.58	22.60±0.03	13.02±0.09
40	28.45±2.90	22.04±0.76	25.10±1.82	25.71±0.15	33.35±0.05	23.03±0.11
60	39.64±0.50	27.35±0.14	34.98±0.79	35.03±0.06	47.68±0.03	33.62±0.09
80	50.59±0.16	38.59±0.40	52.39±0.05	44.61±0.67	58.82±0.00	38.94±0.08
100	66.05±0.69	55.53±0.10	66.61±0.20	60.89±0.71	74.63±0.05	53.61±1.05
IC_{50} (µg/ml)	75.64	98.76	76.72	85.73	63.98	96.16

*Control- Aspirin; % inhibition = 100 x (1-A2/A1); where, A1 = absorbance of the control, A2 = absorbance of the test sample

5.11 In vivo anti-inflammatory activity

The carrageenan-induced paw oedema method was employed to assess the in vivo anti-inflammatory potential of the aqueous extract of *N. herpeticum*. The standard drug (aspirin 100 mg/kg) demonstrated a significant reduction in the paw oedema at all the considered time points after carrageenan administration (**Table 10**). The percentage inhibition of oedema was

found to be 46.67, 75.31, and 88.64 % at 1 hour, 3 hour, and 5 hour, respectively. The groups receiving the aqueous extract of *N. herpeticum* showed a dose- and time-dependent decrease in paw oedema as compared to the control group. The low dose (125 mg/kg) group exhibited a reduction in paw oedema, with an inhibition of paw oedema ranging from 2.22 to 36.36%. Administration of 250 mg/kg aqueous extract showed dose-dependent decreases in the paw oedema at all time intervals, with a maximum inhibition of 45.45% after 5 hours of carrageenan injection. Animals receiving 500 mg/kg dose also showed significant reduction in paw oedema at 1 hr, 3 hr, and 5 hr after carrageenan injection compared to control and the percentage of inhibition of oedema was 20.00%, 51.85%, and 52.27% ($P < 0.001$) at 1, 3 and 5 hr, respectively (**Table 10**).

Table 10 In vivo anti-inflammatory activity of the aqueous extract of *N. herpeticum* in carrageenan-induced paw oedema method. All values are Mean ± SD (n = 6). *P< 0.001 compared to Control [One-way ANOVA followed by Dunnett's multiple comparison test]

Groups	**Paw volume in ml**				**% Inhibition of oedema**		
	0 hr	**1 hr**	**3 hr**	**5 hr**	**1 hr %**	**3 hr %**	**5 hr %**
Control	0.81±0.03	1.26±0.07	1.62±0.05	1.75±0.07	-	-	-
Aspirin 100 mg/kg)	0.82±0.04	1.06±0.06*	1.02±0.03*	0.92±0.06*	46.67	75.31	88.64
Aqueous extract 125 mg/kg	0.81±0.05	1.27±0.02	1.33±0.05*	1.37±0.06*	02.22	35.80	36.36
Aqueous extract 250 mg/kg	0.80±0.03	1.19±0.06*	1.27±0.10*	1.28±0.05*	13.33	41.98	45.45
Aqueous extract 500 mg/kg	0.84±0.03	1.20±0.07*	1.23±0.06*	1.26±0.05*	20.00	51.85	52.27